

This document is confidential and is proprietary to the American Chemical Society and its authors. Do not copy or disclose without written permission. If you have received this item in error, notify the sender and delete all copies.

Reactivity of organoiridium tungsten oxide clusters with transition metal aquo cations

Journal:	<i>Inorganic Chemistry</i>
Manuscript ID	ic-2024-00076m.R2
Manuscript Type:	Article
Date Submitted by the Author:	n/a
Complete List of Authors:	Sugiarto, *; Hiroshima University, Applied Chemistry Mitsubishi, Ryoji; Kanazawa University Sadakane, Masahiro; Hiroshima University, Graduate School of Advanced Science and Engineering

SCHOLARONE™
Manuscripts

Reactivity of organoiridium tungsten oxide clusters with transition metal aquo cations

Sugiarto,^a Ryoji Mitsuhashi,^b and Masahiro Sadakane^{a}*

^aDepartment of Applied Chemistry, Graduate School of Advanced Science and Engineering,
Hiroshima University, 1-4-1 Kagamiyama, Higashi-Hiroshima 739-8527, Japan

^bInstitute of Liberal Arts and Science, Kanazawa University, Kakuma, Kanazawa 920-1192,
Japan

ABSTRACT. Organometallic-polyoxometalate complexes form a unique class of molecular organometallic oxides characterized by the dynamic behavior of the organometallic cations. Herein, we investigated the reactivity of Cp*Ir-octatungstate clusters (where Cp* represents pentamethylcyclopentadienyl, C₅Me₅⁻) with Werner-type transition-metal aquo cations. The addition of Ag⁺, Co²⁺, Ni²⁺, and M³⁺ (M = Cr, Fe, or In) cations to the aqueous solution of Cp*Ir-

octatungstate clusters resulted in the formation of

$[\{ \text{Ag}(\text{OH}_2)_2 \}_2 \{ \text{Cp}^* \text{Ir}(\text{OH}_2) \}_2 \{ \text{Cp}^* \text{IrW}_3\text{O}_{12}(\text{OH}) \}_2 (\text{WO}_2)_2]$ (**1**), $\text{Co}_{1.5}\text{K}_{0.8}\text{Na}_{0.2}[\{ \text{trans-}$

$\text{Co}(\text{OH}_2)_2 \}_2 \{ \text{Cp}^* \text{IrW}_3\text{O}_{12}(\text{OH}) \}_2 (\text{WO}_2)_{1.3} \{ \text{cis-Co}(\text{OH}_2)_2 \}_{0.7}]$ (**2-Co**),

$\text{Ni}_{0.2}\text{K}_{1.4}\text{Na}_{0.2}[\{ \text{Ni}(\text{OH}_2)_4 \}_2 \{ \text{Cp}^* \text{IrW}_3\text{O}_{12}(\text{OH}) \}_2 (\text{WO}_2)_{1.1} \{ \text{cis-Ni}(\text{OH}_2)_2 \}_{0.9}]$ (**2-Ni**), and

$[\{ \text{M}(\text{OH}_2)_4 \}_2 \{ \text{Cp}^* \text{IrW}_3\text{O}_{12}(\text{OH}) \}_2 \{ \text{cis-M}(\text{OH}_2)_2 \}_2] (\text{NO}_3)_2$ ($\text{M} = \text{Cr}$, **3-Cr**; Fe , **3-Fe**; or In **3-In**),

respectively. All clusters share the same cubane-type $\{ \text{Cp}^* \text{IrW}_3\text{O}_{12}(\text{OH}) \}^{5-}$ building block,

representing the first examples of organoiridium-polyoxometalates functionalized by transition-

metal aquo cations. These compounds are insoluble in water, facilitating the evaluation of their

heterogeneous water-oxidation properties. Notably, **2-Co** generates the highest catalytic water

oxidation current. This work provides a new synthetic method to introduce metal-aquo

complexes on an organometallic oxide cluster, producing multimetallic molecules that model

catalytic sites of complex oxides.

Introduction

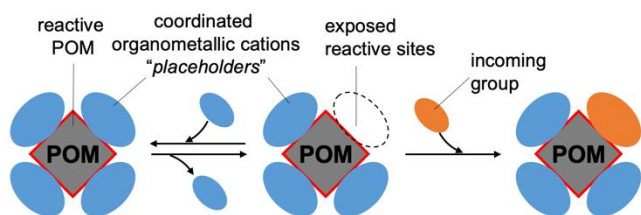
Polyoxometalate (POM) anions are soluble metal-oxide molecules of group 5 (V, Nb, and Ta)

and group 6 (Mo and W) elements. They form various clusters by incorporating hetero groups,

such as template anions and transition-metal cations, into their metal–oxygen backbone.¹⁻³ Our specific focus lies on polyoxometalates capped by multiple metal–carbon fragments, such as {Re(CO)₃},^{4,5} {Ru(arene)},^{6,7} and {Ir(alkene)}.⁸ These organometallic-polyoxometalate (organo-POM) complexes⁹ have attracted considerable interest as potential structural models for the surfaces of heterogeneous catalysts¹⁰ and precursors for synthesizing oxide-supported metal catalysts.¹¹⁻¹³ Functionalization of organo-POMs having readily available coordination sites is crucial because these sites facilitate catalytic reactions and further modification of organo-POMs with various ligands. As such, there is a need to develop a method that allows incorporation of transition metal complexes with available association sites for the binding of various incoming ligands.

Owing to the inherent lability of the coordination bonds connecting organometallic cations and POM anions, the organometallic fragments of organo-POMs exhibit dynamic behavior in solution.¹⁴⁻¹⁷ They can pivot^{18, 19} on the surfaces of the POM or detach²⁰ from the POM in response to external stimuli—such as solvents and temperature—while preserving the POM structure. This unique property, wherein the organometallic cation can dissociate from the POM, makes organo-POMs attractive as building blocks for synthesizing multimetallic-oxide clusters.

For example, Isobe and coworkers reported that the $\{\text{Cp}^*\text{Rh}\}^{2+}$ units (Cp^* is C_5Me_5^-) of $[\{\text{Cp}^*\text{Rh}\}_4\text{V}_6\text{O}_{19}]$ dissociate in an acidic solution and addition of $[\text{Cp}^*\text{Ir}(\text{OH}_2)_3]^{2+}$ into the solution produces a series of $[\{\text{Cp}^*\text{Rh}\}_{4-x}\{\text{Cp}^*\text{Ir}\}_x\text{V}_6\text{O}_{19}]$ clusters where x can take values of 1, 2, 3, or 4.²¹ In other words, the organometallic cations of organo-POMs function as a protecting^{22, 23} or placeholder group²⁴ by temporarily blocking the reactive sites of a POM anion, and they are exchangeable to other incoming metal cations (Scheme 1). We were thus motivated to exploit this substitution reaction to functionalize organo-POMs with simple transition metal-aquo complexes that can provide association sites for various incoming ligands.



Scheme 1. Cation exchange reaction of an organo-POM

Recently, we reported that the reaction of $[(\text{Cp}^*\text{IrCl})_2(\mu\text{-Cl})_2]$ and Na_2WO_4 in aqueous solutions produces a highly nucleophilic octatungstate $[\{\text{W}_3\text{O}_{12}(\text{OH})\}_2(\text{WO}_2)_2]^{10-}$ anion, which is capped by multiple $\{\text{Cp}^*\text{Ir}\}^{2+}$ fragments (Scheme 2).²⁵ Our question was whether the $\{\text{Cp}^*\text{Ir}\}^{2+}$ cations are substitutable to Werner-type transition-metal aquo cations. Herein, we demonstrate that the addition of Ag^+ , Co^{2+} , Ni^{2+} , and M^{3+} ($\text{M} = \text{Cr}, \text{Fe}, \text{or In}$) cations into the

aqueous solution of Cp*Ir-octatungstate clusters produces

$[\{ \text{Ag}(\text{OH}_2)_2 \}_2 \{ \text{Cp}^*\text{Ir}(\text{OH}_2) \}_2 \{ \text{Cp}^*\text{IrW}_3\text{O}_{12}(\text{OH}) \}_2 (\text{WO}_2)_2]$ (**1**), $\text{Co}_{1.5}\text{K}_{0.8}\text{Na}_{0.2}[\{ \text{trans-}$

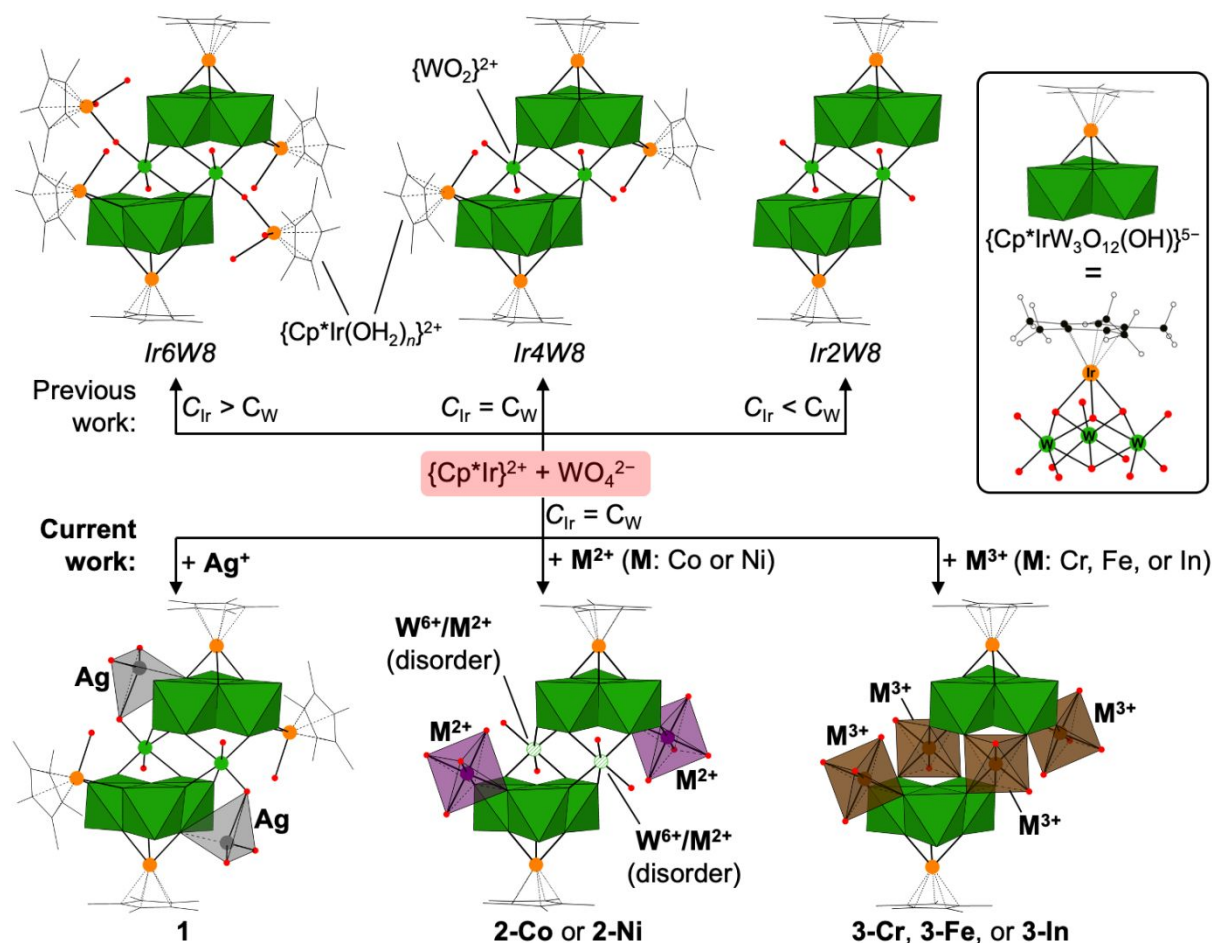
$\text{Co}(\text{OH}_2)_2 \}_2 \{ \text{Cp}^*\text{IrW}_3\text{O}_{12}(\text{OH}) \}_2 (\text{WO}_2)_{1.3} \{ \text{cis-Co}(\text{OH}_2)_2 \}_{0.7}]$ (**2-Co**),

$\text{Ni}_{0.2}\text{K}_{1.4}\text{Na}_{0.2}[\{ \text{Ni}(\text{OH}_2)_4 \}_2 \{ \text{Cp}^*\text{IrW}_3\text{O}_{12}(\text{OH}) \}_2 (\text{WO}_2)_{1.1} \{ \text{cis-Ni}(\text{OH}_2)_2 \}_{0.9}]$ (**2-Ni**), and

$[\{ \text{M}(\text{OH}_2)_4 \}_2 \{ \text{Cp}^*\text{IrW}_3\text{O}_{12}(\text{OH}) \}_2 \{ \text{cis-M}(\text{OH}_2)_2 \}_2] (\text{NO}_3)_2$ ($\text{M} = \text{Cr}$, **3-Cr**; Fe , **3-Fe**; or In **3-In**),

respectively (Scheme 2). These compounds are insoluble in water, and we investigated their

heterogeneous water-oxidation properties.



Scheme 2. Reaction scheme showing our previous work on the molar-ratio-dependent coordination of $\{\text{Cp}^*\text{Ir}\}^{2+}$ to an octatungstate anion and current work on the competitive binding of $\{\text{Cp}^*\text{Ir}\}^{2+}$ and Werner-type metal-aquo cations onto polyoxotungstate. Green, orange, and red circles represent tungsten, iridium, and oxygen atoms, respectively. Cp^* ligands are shown as black sticks. Green octahedra represent W-O_6 octahedra. Inset: structure of the $\{\text{Cp}^*\text{IrW}_3\text{O}_{12}(\text{OH})\}^{5-}$ building block.

Experimental Section

Materials and methods. Chemicals were purchased and used as received. Homemade distilled water was used (Elix, Essential). Fourier transform infrared (FTIR) spectra were collected using a KBr disc on a ThermoFisher Scientific Nicolet 6700 FTIR spectrometer. Powder X-ray diffraction (PXRD) patterns were collected using a Bruker D2 Phaser ($\text{Cu K}\alpha$ radiation, $\lambda = 1.54184 \text{ \AA}$) equipped with a 1D Lynxeye detector. ^1H NMR spectra were recorded on a Variant System 500 (500 MHz; H resonance frequency = 499.827 MHz) spectrometer at ambient temperature, and chemical shifts were referred to the residual solvent signal of $(\text{CD}_3)_2\text{SO}$ at $\delta =$

2.48 ppm. Thermogravimetric analyses (TGA) were performed using a Hitachi SII TG/DTA7300 analyzer with a heating rate of 10 °C/min under a constant air flow of 200 mL/min. Magnetic susceptibility data were recorded using an MPMS-7 SQUID magnetometer in the temperature range of 1.9–300 K. All data were corrected for diamagnetism of the samples by means of Pascal's constants. Total elemental (nonoxygen) analyses of **1**, **2-Co**, and **3-Fe** were performed by Mikroanalytisches Labor Pascher University (Remagen, Germany), whereas CHN elemental analyses of **3-Cr** and **3-In** were performed by the Division of Instrumental Analysis at Okayama University.

Synthesis of $[\{Ag(OH_2)_2\}_2\{Cp^*Ir(OH_2)\}_2\{Cp^*IrW_3O_{12}(OH)_2(WO_2)_2\} \cdot nH_2O$ (1**).**

$[(Cp^*IrCl)_2(\mu-Cl)_2]$ (20.2 mg; 0.025 mmol) was dissolved in 0.1 M aqueous $AgNO_3$ (1.0 mL; 0.1 mmol) under vigorous stirring in the dark for 30 min to generate a yellow–green solution (pH = 2.0) of $[Cp^*Ir(OH_2)_3]^{2+}$ cations. The white precipitate of $AgCl$ was discarded by filtration, and $Na_2WO_4 \cdot 2H_2O$ (16.5 mg; 0.05 mmol) was dissolved in the filtrate, giving a deep yellow solution (pH = 5.39). Finally, 0.1 M aqueous $AgNO_3$ (1.0 mL; 0.1 mmol) was added to the solution, and it was finely filtered through a disposable membrane filter (Advantec DISMIC-13HP020AN with a 0.2 μm pore size) before crystallization in the dark. Yellow crystals appeared within

hours, and the crystallization continued overnight. The crystals were rinsed with a few drops of water and dried in the air. Yield = 16.9 mg (33% based on Ir). Anal. Calcd for $n = 25$: C, 11.90; H, 3.10; Ag, 5.35; Ir, 19.05; W, 36.43. Found: C, 12.37; H, 3.06; Ag, 4.86; Ir, 19.2; W, 36.2; Cl, <0.1; N, <0.1. TGA up to 650 °C (Figure S1 in the Supporting Information) revealed a 26.19% weight decrease, corresponding to the decomposition of one mole of **1** to $4\text{IrO}_2 \cdot 8\text{WO}_3 \cdot 2\text{Ag}$ (calcd 26.17% for $n = 24$). ^1H NMR (in $(\text{CD}_3)_2\text{SO}$, δ/ppm): 1.78 (s, 15H), 1.64 (s, 15H), corresponding to the signals of free $[\{\text{Cp}^*\text{Ir}\}_2\{\text{Cp}^*\text{Ir}(\text{OH}_2)\}_2\{\text{Cp}^*\text{IrW}_3\text{O}_{12}(\text{OH})_2(\text{WO}_2)_2\}]^{2-}$ anions produced from the de-coordination of Ag^+ from **1**. FTIR (KBr disc, $1500\text{--}700\text{ cm}^{-1}$ region, v/cm^{-1}): 1456, 1385, 1030, 928, 897, 872, 820, 758 (refer to Figure S2 for the full FTIR spectra of all compounds).

Synthesis of $\text{Co}_{1.5}\text{K}_{0.8}\text{Na}_{0.2}[\{\text{trans-Co}(\text{OH}_2)_2\}\{\text{Cp}^*\text{IrW}_3\text{O}_{12}(\text{OH})_2(\text{WO}_2)_{1.3}\{\text{cis-Co}(\text{OH}_2)_2\}_{0.7}\} \cdot n\text{H}_2\text{O}$ (2-Co). $[(\text{Cp}^*\text{IrCl})_2(\mu\text{-Cl})_2]$ (20.0 mg; 0.025 mmol) and $\text{Na}_2\text{WO}_4 \cdot 2\text{H}_2\text{O}$ (16.5 mg; 0.05 mmol) were mixed in 0.1 M potassium acetate (2.0 mL), and the suspension was stirred on a hotplate at 80 °C for 10–15 min to produce a clear yellow solution ($\text{pH} = 6.3$). The solution was cooled to room temperature, and $\text{CoSO}_4 \cdot 7\text{H}_2\text{O}$ (28.0 mg; 0.1 mmol) was added and dissolved with gentle shaking to give a clear solution ($\text{pH} = 5.98$). The solution was sealed in a

glass vial and put in a drying oven set at 70 °C for crystallization. Crystals were formed after several hours and were harvested after standing overnight. The crystals were rinsed with a few drops of water and dried in the air. Yield = 13.3 mg (17% based on Ir). Anal. Calcd for $n = 20$: C, 7.74; H, 2.57; Co, 6.08; Ir, 12.39; K, 1.01; Na, 0.15; W, 43.25. Found: C, 7.37; H, 2.96; Co, 5.84; Ir, 12.2; K, 1.08; Na, 0.12; W, 43.4; Cl, < 0.05; S, 0.028. Crystals of **2-Co** easily lost their water of crystallization at ambient temperature, and the number of crystallizations varied depending on the age of the sample: TGA up to 600 °C (Figure S3) of freshly prepared crystals and five-day-aged crystals (at 27 °C in a sealed tube) revealed a 27.52% and 23.5% decrease in weight, respectively, corresponding to the decomposition of one mole of **2-Co** to $2\text{IrO}_2 \cdot 7.3\text{WO}_3 \cdot 3.2\text{CoO} \cdot 0.4\text{K}_2\text{O} \cdot 0.1\text{Na}_2\text{O}$ (calcd 27.73% for $n = 34$ and 23.62% for $n = 24$). FTIR (KBr disc, 1500–700 cm^{-1} region, v/cm^{-1}): 1456, 1385, 1030, 918, 827, 723 (Figure S2).

Synthesis of $\text{Ni}_{0.2}\text{K}_{1.4}\text{Na}_{0.2}[\{\text{Ni}(\text{OH}_2)_4\}_2\{\text{Cp}^*\text{IrW}_3\text{O}_{12}(\text{OH})\}_2(\text{WO}_2)_{1.1}\{\text{cis-Ni}(\text{OH}_2)_2\}_{0.9}]\cdot n\text{H}_2\text{O}$ (2-Ni**).** $[(\text{Cp}^*\text{IrCl})_2(\mu\text{-Cl})_2]$ (20.0 mg; 0.025 mmol) and $\text{Na}_2\text{WO}_4 \cdot 2\text{H}_2\text{O}$ (16.5 mg; 0.05 mmol) were mixed in 0.1 M potassium acetate (2.0 mL), and the suspension was stirred on a hotplate at 80 °C for 10–15 min to produce a clear yellow solution. The solution was cooled to room temperature (20–22 °C), and $\text{NiNO}_3 \cdot 6\text{H}_2\text{O}$ (29.2 mg; 0.1 mmol) was added to give a clear

solution. Crystallization at 27 °C overnight produced a few green crystals. The crystals were rinsed with a few drops of water and dried in the air. Yield = 6.0 mg (7% based on Ir). Anal. Calcd for $n = 40$: C, 6.76; H, 3.74; Ir, 10.82; K, 1.54; Na, 0.13; Ni, 5.12; W, 36.74. Found: C, 7.19; H, 3.32; Ir, 10.8; K, 1.28; Na, 0.12; Ni, 5.14; W, 36.7; Cl, < 0.05. Crystals of **2-Ni** easily lost their water of crystallization at ambient temperature; TGA up to 619 °C (Figure S4) found a 26.96% decrease in weight, corresponding to the decomposition of one mole of **2-Ni** to $2\text{IrO}_2 \cdot 7.1\text{WO}_3 \cdot 3.1\text{NiO} \cdot 0.7\text{K}_2\text{O} \cdot 0.1\text{Na}_2\text{O}$ (calcd 26.94% for $n = 26$). FTIR (KBr disc, 1500–700 cm^{-1} region, v/cm^{-1}): 1456, 1385, 1032, 920, 843, 748 (Figure S2).

Synthesis of $[\{\text{Fe}(\text{OH}_2)_4\}_2\{\text{Cp}^*\text{IrW}_3\text{O}_{12}(\text{OH})\}_2\{\text{cis-Fe}(\text{OH}_2)_2\}_2](\text{NO}_3)_2 \cdot n\text{H}_2\text{O}$ (**3-Fe**).

$[(\text{Cp}^*\text{IrCl})_2(\mu\text{-Cl})_2]$ (20.2 mg; 0.025 mmol) was dissolved in 0.1 M aqueous AgNO_3 (1.0 mL; 0.1 mmol) under vigorous stirring in the dark for 30 min to generate a yellow–green solution of $[\text{Cp}^*\text{Ir}(\text{OH}_2)_3]^{2+}$ cations. The white precipitate of AgCl was discarded by filtration, and $\text{Na}_2\text{WO}_4 \cdot 2\text{H}_2\text{O}$ (49.4 mg; 0.15 mmol) was dissolved in the filtrate to give a yellow solution (pH = 7.74). Then, $\text{Fe}(\text{NO}_3)_3 \cdot 9\text{H}_2\text{O}$ (40.4 mg; 0.1 mmol) was added in one portion to the solution, forming copious brown solids that redissolved within 1–2 min of manual stirring. The clear, deep red solution (pH = 1.70) was finely filtered through a disposable membrane filter (Advantec

DISMIC-13HP020AN with a 0.2 μm pore size) before crystallization. Red-brown crystals were deposited within an hour and harvested after standing overnight. The crystals were rinsed several times with water and dried in the air. Yield = 59.5 mg (76% based on Ir). Anal. Calcd for $n=18$: C, 7.84; H, 3.03; Fe, 7.29; Ir, 12.55; N, 0.91; W, 36.0. Found: C, 7.73; H, 2.98; Fe, 7.14; Ir, 12.0; N, 0.79; W, 36.4; Na, < 0.01; Cl, < 0.1; Ag, < 0.05. TG analysis up to 570 $^{\circ}\text{C}$ (Figure S5) found a 28.3% decrease in weight corresponding to the decomposition of one mole of **3-Fe** to $2\text{Fe}_2\text{O}_3 \cdot 2\text{IrO}_2 \cdot 6\text{WO}_3$ (calcd 28.28% for $n=15$). FTIR (KBr disc, 1500–700 cm^{-1} region, v/cm^{-1}): 1385 (NO_3^-), 1032, 933, 856, 816, 766 (Figure S2); the vibrations of Cp^* ligands (1500–1400 cm^{-1} were obscured by the broad and strong vibration of the nitrate anion at 1385 cm^{-1}).

Synthesis of $[\{\text{M}(\text{OH}_2)_4\}_2\{\text{Cp}^*\text{IrW}_3\text{O}_{12}(\text{OH})_2\}\{\text{cis-M}(\text{OH}_2)_2\}_2](\text{NO}_3)_2 \cdot n\text{H}_2\text{O}$ ($\text{M} = \text{Cr}$, **3-Cr or **In**, **3-In**).** $[(\text{Cp}^*\text{IrCl})_2(\mu\text{-Cl})_2]$ (20.2 mg; 0.025 mmol) was dissolved in 0.1 M aqueous AgNO_3 (1.0 mL; 0.1 mmol) under vigorous stirring in the dark for 30 min to generate a yellow–green solution of $[\text{Cp}^*\text{Ir}(\text{OH}_2)_3]^{2+}$ cations. The white precipitate of AgCl was discarded by filtration, and $\text{Na}_2\text{WO}_4 \cdot 2\text{H}_2\text{O}$ (16.5 mg; 0.05 mmol) was dissolved in the filtrate to give a yellow solution. Then, $\text{Cr}(\text{NO}_3)_3 \cdot 6\text{H}_2\text{O}$ (100 mg; 0.25 mmol) or $\text{In}(\text{NO}_3)_3 \cdot 3\text{H}_2\text{O}$ (88.5 mg; 0.25 mmol) was added in one portion to the solution, forming a deep green solution for Cr^{3+} (or a yellow solution for

In³⁺). The solution was filtered through a disposable membrane filter (Advantec DISMIC-13HP020AN with a 0.2 μm pore size) before crystallization at 27 °C for 2 d. The deposited green crystals were rinsed several times with water and dried in the air. Characterization for **3-Cr**: Yield = 5.8 mg (8% based on Ir). Anal. Calcd for $n = 18$: C, 7.88; H, 3.05; N, 0.92. Found: C, 7.61; H, 3.04; N, 0.8. TG analysis up to 447 °C (Figure S5) found a 28.0% decrease in weight corresponding to the decomposition of one mole of **3-Cr** to $2\text{Cr}_2\text{O}_3 \cdot 2\text{IrO}_2 \cdot 6\text{WO}_3$ (calcd 27.99% for $n = 14$). FTIR (KBr disc, 1500–700 cm^{-1} region, ν/cm^{-1}): 1385 (NO_3^-), 1034, 928, 867, 831, 783 (Figure S2). Characterization for **3-In**: Yield = 21.8 mg (26% based on Ir). Anal. Calcd for $n = 18$: C, 7.28; H, 2.82; N, 0.85. Found: C, 7.29; H, 2.7; N, 0.77. TG analysis up to 656 °C (Figure S5) found a 27.6% decrease in weight corresponding to the decomposition of one mole of **3-In** to $2\text{In}_2\text{O}_3 \cdot 2\text{IrO}_2 \cdot 6\text{WO}_3$ (calcd 27.43% for $n = 18$). FTIR (KBr disc, 1500–700 cm^{-1} region, ν/cm^{-1}): 1385 (NO_3^-), 1030, 931, 864, 825 (Figure S2).

Solid-state electrochemistry. The water-oxidation properties of the compounds were studied in the solid state using the carbon-paste technique.²⁶ All voltammograms were recorded using an ALS/CH electrochemical analyzer model 620D. In a typical experiment, the working electrode containing 10 wt% of the sample was prepared by mixing carbon paste (BAS, Carbon Paste Oil

Base, 45 mg) and the analyte (5 mg) and thoroughly grinding using a mortar. The resulting paste was loaded into a hollow electrode and polished on glassine weighing paper until the surface was firm and smooth. The diameter of the active electrode was 0.3 cm, which corresponded to an active surface area of 0.07 cm². The reference and counter electrodes were Ag/AgCl in 3 M NaCl and platinum wire, respectively. The electrolyte was a 0.05 M sodium phosphate solution at pH 7 (prepared by dissolving a calculated amount of NaH₂PO₄ and adjusting the final pH to 7.0 using 1 M aqueous NaOH) with additional NaNO₃ (for a total concentration of 1 M). The solution was purged using nitrogen gas before data collection, and the cyclic voltammograms were recorded under a nitrogen atmosphere. The scan was started at the open-circuit potential and swept towards the positive potential at a scan rate of 0.1 V/s. Controlled-potential electrolysis experiments were conducted in a 0.05 M sodium phosphate solution at pH 7 (without additional NaNO₃) using a constant potential of +1.1 V (vs. Ag/AgCl).

X-ray crystallography. A single crystal suitable for X-ray diffraction was suspended in mineral oil and mounted on a goniometer head under a nitrogen stream. Intensity data were collected at – 150 °C on a Bruker SMART APEXII diffractometer equipped with a CCD detector and Mo K α radiation ($\lambda = 0.71073 \text{ \AA}$) source monochromated by layered confocal mirrors. Data reduction,

integration, and scaling were performed on a Bruker APEX3 suite.²⁷ The intensities were corrected against absorption using SADABS.²⁷ The initial structure was determined using the SHELXT²⁸ program and subsequently refined using SHELXL²⁹ running on a ShelXle³⁰ user interface. Some disordered crystallization water was removed using the Platon SQUEEZE tool.³¹ All the non-hydrogen atoms were refined anisotropically. The hydrogen atoms of the Cp* ligands were generated at the calculated positions using a riding model. The detailed crystallographic parameters are summarized in Table S1. The crystal data of **3-Cr** is of low quality, and hence, the bond parameters are imprecise; there are ghost peaks around all of the metal atoms, and strong SIMU, DELU, and ISOR were needed to prevent the chromium atoms from going nonpositive definite.

There was a substitutional disorder in **2-Co** and **2-Ni**, wherein the *cis*-{WO₂}²⁺ fragments were partially substituted for *cis*-{M(OH₂)₂}²⁺ (M = Co or Ni). This disorder was evidenced by the atomic displacement parameters and bond distances as follows: (i) The W atom of the *cis*-{WO₂}²⁺ (W_{WO2}, for short) sits on the special position (*C*₂ axis, with a special position constraint on the site occupancy of 0.5), and the initial structure with this 0.5 occupancy of the W_{WO2} in the isotropic model showed significantly larger *U*_{iso} of W_{WO2} compared to that of other W atoms.

The $F_o - F_c$ map showed a negative density at the W_{WO_2} site, signaling partial occupancy of W_{WO_2} . (ii) The terminal W_{WO_2} -O bond length was 1.87 Å, which is too long for the expected distance of terminal W=O bonds (approximately 1.7 Å). The bond distance is reasonable for the average distance between terminal W=O and M^{II} -OH₂ bonds (the common M^{II} -OH₂ bond length is approximately 2.0–2.1 Å). This substitutional disorder was refined using the PART command in combination with EXYZ and EADP restraints so that both W_{WO_2} and M^{II} sit on the same atomic coordinates and have the same atomic displacement parameters. Their occupancies were refined by setting the second free variable FVAR, and the obtained values were: (i) 0.3163 for W_{WO_2} and 0.1837 for Co^{II} in **2-Co** and (ii) 0.2663 for W_{WO_2} and 0.2337 for Ni^{II} in **2-Ni**. These results were in good agreement with the atomic ratio found by elemental analyses: Ir:W:Co = 2:7.4:3.1 and Ir:W:Ni = 2:7.1:3.1 corresponding to the chemical formula of $Co_{1.5}K_{0.8}Na_{0.2}[\{trans-Co(OH_2)_2\}\{Cp^*IrW_3O_{12}(OH)\}_2(WO_2)_{1.3}\{cis-Co(OH_2)_2\}_{0.7}]\cdot 20H_2O$ and $Ni_{0.2}K_{1.4}Na_{0.2}[\{Ni(OH_2)_4\}_2\{Cp^*IrW_3O_{12}(OH)\}_2(WO_2)_{1.1}\{cis-Ni(OH_2)_2\}_{0.9}]\cdot 40H_2O$, respectively. Because both $cis-\{WO_2\}^{2+}$ and $cis-\{M(OH_2)_2\}^{2+}$ have the same cationic charges, the partial substitution does not affect the total charge of the cluster. Owing to a severe disorder, the exact numbers of the countercations could not be located in the crystal structure.

Bond valence sum (BVS) calculation. The BVS values were calculated using the expression for the variation of length r_{ij} of a bond between two atoms, i and j , in an observed crystal with valence V_i .³²

$$V_i = \sum_j \exp \left(\frac{r'_0 - r_{ij}}{B} \right),$$

where B is a constant equal to 0.37 Å (except for Ir, where it is 0.414 Å), and r'_0 is the bond valence parameter for a given atom pair. To calculate the BVS values of the metal and oxygen atoms, we used r'_0 (in Å) = 1.906 for W⁶⁺–O, 1.755 for Ir³⁺–O, 1.842 for Ag⁺–O, 1.692 for Co²⁺–O, 1.654 for Ni²⁺–O, 1.724 for Cr³⁺–O, 1.753 for Fe³⁺–O, and 1.902 for In³⁺–O. The results of the BVS calculations are tabulated in Table S2.

Results and Discussion

Synthesis and structure

The addition of AgNO₃ to an aqueous mixture of [Cp*Ir(OH₂)₃]²⁺ (generated in situ by reacting one portion of [(Cp*IrCl)₂(μ-Cl)₂] with four portions of AgNO₃ in water) and Na₂WO₄ in a 2:1:1 Ag⁺/(Cp*Ir)²⁺/WO₄²⁻ mixing ratio produced compound **1**. As shown in Figure 1a, **1**

consists of a tetra-(Cp*Ir)-grafted octatungstate [$\{\text{Cp}^*\text{Ir}(\text{OH}_2)\}_2(\text{Cp}^*\text{Ir})_2\text{H}_2\text{W}_8\text{O}_{30}\text{]}^{2-}$ (Ir_4W_8 , see Scheme 2) anionic core with two additional $\{\text{Ag}(\text{OH}_2)_2\}^+$ fragments, and hence **1** is a charge-neutral complex. The Ir_4W_8 anion has been reported by Niu et al.³³ and recently by us²⁵ and is made up of cubane-type $\{\text{Cp}^*\text{IrW}_3\text{O}_{12}(\text{OH})\}^{5-}$, bridging $\text{cis-}\{\text{WO}_2\}^{2+}$, and dangling $\{\text{Cp}^*\text{Ir}(\text{OH}_2)\}^{2+}$ fragments; the $\{\text{Cp}^*\text{IrW}_3\text{O}_{12}(\text{OH})\}^{5-}$ fragment is also the building units in **2-Co**, **2-Ni**, **3-Cr**, **3-Fe** and **3-In**, see below.

The $\{\text{Ag}(\text{OH}_2)_2\}^+$ cation is coordinated to Ir_4W_8 through one of the terminal oxygen atoms (O12) of the $\text{cis-}\{\text{WO}_2\}^{2+}$ ($d\text{Ag1-O12} = 2.445 \text{ \AA}$) and one of the μ_3 -oxygen atoms (O5) of the $\{\text{Cp}^*\text{IrW}_3\text{O}_{12}(\text{OH})\}^{5-}$ cube ($d\text{Ag1-O5} = 2.486 \text{ \AA}$). The two terminal oxygen atoms (O17 and O18) on Ag1 are aquo ligands, as confirmed by the bond distances ($d\text{Ag1-O17} = 2.358$ and $d\text{Ag1-O18} = 2.310 \text{ \AA}$) and their bond valence sum (BVS) values (O17 = 0.25 and O18 = 0.28). A weak interaction exists between Ag1 and one of the methyl groups of Cp* bound to Ir1 ($d\text{Ag1}\cdots\text{C} = 3.34 \text{ \AA}$),³⁴⁻³⁶ and this interaction significantly distorts the coordination geometry of Ag1 from normal tetrahedral angles. Many silver-containing polyoxometalates are synthesized in organic media wherein silver is coordinated by polyoxometalate anions and organic solvents such as acetonitrile and amides with typical coordination numbers of 4–6.³⁷ The structure of

silver cation in aqueous solution has been intensively studied, and EXAFS results indicate tetrahedral $[\text{Ag}(\text{OH}_2)_4]^+$ with two short (2.32 Å) and two long (2.54 Å) Ag–O bond lengths.³⁸ As such, the coordination geometry of the $\{\text{Ag}(\text{OH}_2)_2\}^+$ units in **1** provides solid-state evidence of the structure of solvated silver cations.

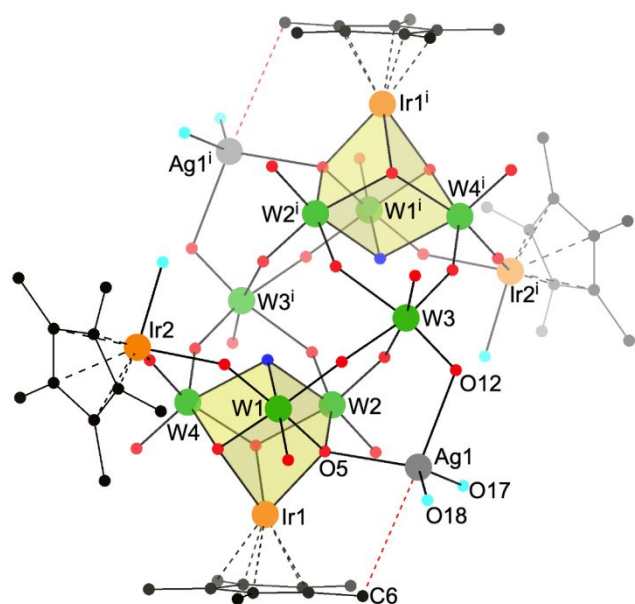


Figure 1. Structure of **1**. The dashed red lines show the weak interaction between Ag and one of the methyl groups of Cp*. The yellow translucent cubes emphasize the cubane-type {IrW₃O₄} building blocks. Color scheme: green, W; orange, Ir; gray, Ag; red, O; blue, OH groups; cyan, OH₂ ligands; black, C. The hydrogen atoms are omitted for clarity. Symmetry operation: (i) $-x, -y, -z$.

Compound **1** is insoluble in water but dissolves in dimethyl sulfoxide, and its ^1H NMR spectrum (Figure S6) in $(\text{CD}_3)_2\text{SO}$ showed two singlets at 1.78 and 1.66 ppm with an integration ratio of 1:1 corresponding to the protons of the methyl groups of the $\{\text{Cp}^*\text{Ir}(\text{OH}_2)\}^{2+}$ and $\{\text{Cp}^*\text{Ir}\}^{2+}$ fragments, respectively. To confirm whether the $\{\text{Ag}(\text{OH}_2)\}^{2+}$ cations remained coordinated or dissociated upon dissolution, we compared the ^1H NMR spectra of a dimethyl sulfoxide solution of **1** and $[(\text{Cp}^*\text{Ir})(\mu\text{-OH})_3]_2(\text{Ir}_4\text{W}_8)$, which contained the noncoordinating $[(\text{Cp}^*\text{Ir})(\mu\text{-OH})_3]^+$ cations. Their spectra were identical (Figure S6), indicating that the silver-aquo groups dissociated from the cluster upon dissolution.

The addition of $\text{CoSO}_4 \cdot 7\text{H}_2\text{O}$ to a mixture of $[(\text{Cp}^*\text{IrCl})_2(\mu\text{-Cl})_2]$ and Na_2WO_4 in 0.1 M aqueous CH_3COOK solution in 2:1:1 $\text{Co}^{2+}/(\text{Cp}^*\text{Ir})^{2+}/\text{WO}_4^{2-}$ mixing ratio produced **2-Co**. The use of CoSO_4 was necessary to obtain single crystals suitable for X-ray diffraction; syntheses using $\text{Co}(\text{NO}_3)_2$ gave smaller crystals whose PXRD pattern was similar to that of **2-Co** (Figure S7). Compound **2-Co** crystallized in the orthorhombic space group *Pmma*, with one-fourth of the molecule in the asymmetric unit. The anionic part of **2-Co** forms a one-dimensional chain structure, and a segment of the chain is given in Figure 2a. The chain comprises a repeating unit of $[\{ \textit{trans}\text{-Co}(\text{OH}_2)_2 \} \{ \text{Cp}^*\text{IrW}_3\text{O}_{12}(\text{OH}) \}_2 (\textit{cis}\text{-WO}_2)_{1.3} \{ \textit{cis}\text{-Co}(\text{OH}_2)_2 \}_{0.7}]^{4-}$ wherein the *trans*-

{Co(OH₂)₂}²⁺ (Co1) functions as the linker, connecting one unit to another by forming coordination bonds to O3 (*d*Co1–O3 = 2.085 Å). The shape of the resulting chain resembles a sinusoidal waveform and propagates along the [100] direction. Note that approximately 35% of the *cis*-{WO₂}²⁺ fragments are substituted with *cis*-{Co(OH₂)₂}²⁺, and their refinement is detailed in the X-ray crystallography section. BVS calculations indicate that Co1 is in a +2 oxidation state, and the two coordinated oxygen atoms are water molecules. The *trans*-{Co(OH₂)₂}²⁺ cation contains long Co1–O10 (*d* = 2.21 Å) and shorter Co1–O11 (*d* = 2.08 Å) bonds; a Co²⁺–OH₂ bond distance as long as 2.24 Å is known.³⁹ In the crystal packing, the chains are connected by pi stacking (*d* = 3.51 Å, measured from the centroid of the Cp* rings) of the Cp* rings, forming supramolecular sheets on the crystallographic *ac* plane (Figure 2b). Recently, Abramov and co-workers reported that pi interactions in (benzene)ruthenium-polyoxotungstate are tunable by changing pH of the crystallization solution.⁴⁰ As such, Cp*Ir-containing polyoxometalates are attractive building blocks for the engineering of crystal structures.

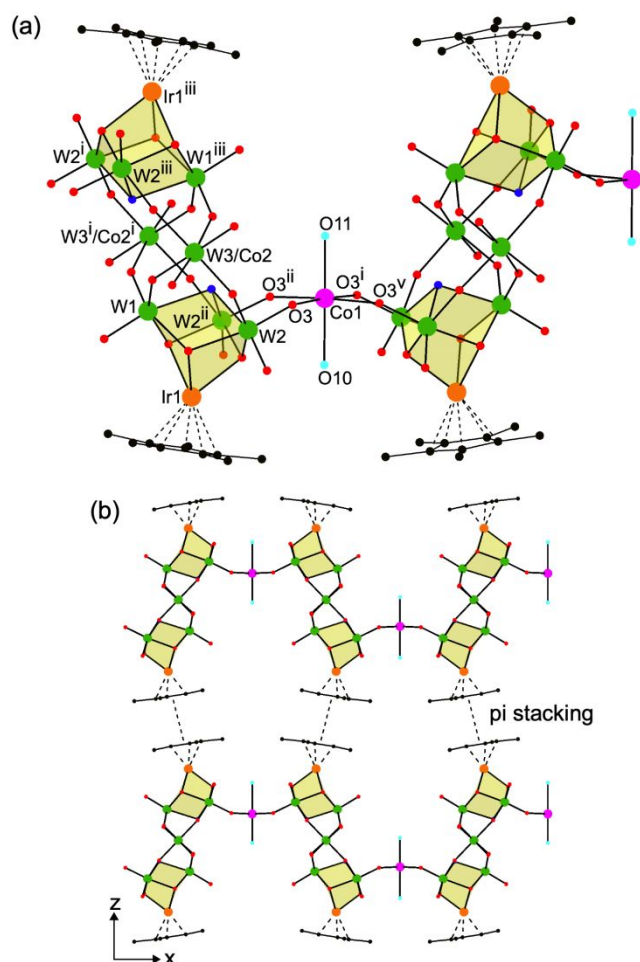
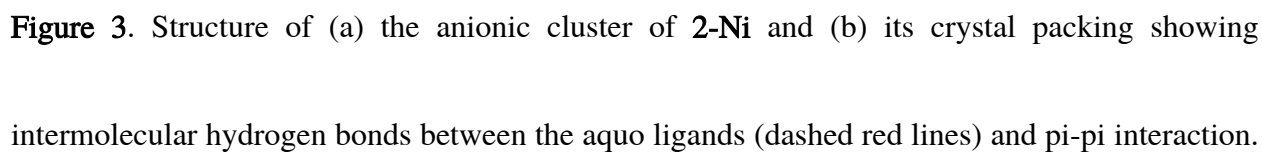


Figure 2. (a) Segment of the chain structure of the anionic part of **2-Co** and (b) its crystal packing projected along the crystallographic b axis showing interchain pi stacking. Color scheme: green, W; orange, Ir; magenta, Co; red, O; blue, OH groups; cyan, OH₂ ligands; black, C. The hydrogen atoms are omitted for clarity. Symmetry operation: (i) $-x, -y, -z$; (ii) $x, -y, z$; (iii) $-x, y, -z$; (iv) $\frac{1}{2}-x, -y, z$; (v) $\frac{1}{2}-x, y, z$.

By contrast, the addition of Ni(NO₃)₂·6H₂O to a mixture of [(Cp*IrCl)₂(μ-Cl)₂] and Na₂WO₄ in 0.1 M aqueous CH₃COOK solution in 2:1:1 Ni²⁺/(Cp*Ir)²⁺/WO₄²⁻ mixing ratio gave a discrete

nickel-coordinated cluster $\text{Ni}_{0.2}\text{K}_{1.4}\text{Na}_{0.2}[\{\text{Ni}(\text{OH}_2)_4\}_2\{\text{Cp}^*\text{IrW}_3\text{O}_{12}(\text{OH})\}_2(\text{WO}_2)_{1.1}\{\text{cis-}$
 $\text{Ni}(\text{OH}_2)_2\}_{0.9}]^{2-}$ (**2-Ni**), isolated in a low yield and low reproducibility. As shown in Figure 3a,
the structure comprises a Cp^*Ir -polyoxotungstate core and two $\{\text{Ni}(\text{OH}_2)_2\}^{2+}$ fragments. BVS
calculations indicate Ni1 is in a +2 oxidation state, and its terminal oxygen atoms (O9, O11, and
O12) are water molecules with an average Ni–OH₂ bond distance of 2.083 Å. The reason why **2-**
Ni form discrete anion is perhaps caused by the slower (i.e., 100 times slower) ligand exchange
rate of Ni^{II}–aquo cations (k at 298 K = $3.2 \times 10^4 \text{ s}^{-1}$) compared to that of Co^{II}–aquo cations (k at
298 K = $3.2 \times 10^6 \text{ s}^{-1}$).⁴¹ In the crystal packing (Figure 3b), the discrete anions interact with each
other through intermolecular hydrogen bonds ($d\text{O9}\cdots\text{O9} = 2.74 \text{ Å}$ and $d\text{O12}\cdots\text{O3} = 2.73 \text{ Å}$) and
pi-stacking (centroid-to-centroid distance = 3.6 Å).



Color scheme: green, W; orange, Ir; purple, Ni; red, O; blue, protonated O (OH^-); cyan, O of aquo ligands; black, C. Symmetry operation: (i) $-x, -y, -z$; (ii) $x, -y, z$; (iii) $-x, y, -z$.

The addition of $\text{Fe}(\text{NO}_3)_3 \cdot 9\text{H}_2\text{O}$ to a mixture of $\{\text{Cp}^*\text{Ir}(\text{OH}_2)_3\}^{2+}$ and Na_2WO_4 in a 2:1:3 $\text{Fe}^{3+}/(\text{Cp}^*\text{Ir})^{2+}/\text{WO}_4^{2-}$ mixing ratio gave **3-Fe**. Compound **3-Fe** also formed in the 1:1:1 and 5:1:1 mixing ratios; however, the 2:1:3 mixture always gave the highest yield. Similar compounds but with Cr^{3+} (**3-Cr**) or In^{3+} (**3-In**) instead were obtained from the 5:1:1 mixture of $\text{M}(\text{NO}_3)_3$ ($\text{M} = \text{Cr}$ or In), $\{\text{Cp}^*\text{Ir}(\text{OH}_2)_3\}^{2+}$, and Na_2WO_4 . These compounds are isostructural, and **3-Fe** is discussed. Unlike **1** and **2-Co** (or **2-Ni**), which are *charge-neutral* and *anionic* organo-POMs, **3-Fe** is a *cationic* organo-POM compensated by NO_3^- . The presence of NO_3^- was confirmed by a sharp IR band at 1385 cm^{-1} , elemental analysis, and single crystal X-ray structure analysis. The structure of the cation is shown in Figure 4a, and it comprises the $\{\text{Cp}^*\text{IrW}_3\text{O}_{12}(\text{OH})\}^{5-}$ anions as the principal building units and four iron-aquo cations. Two of the iron-aquo groups are *cis*- $\{\text{Fe}(\text{OH}_2)_2\}^{3+}$ cations (Fe1, O14, and O15), and they connect the two $\{\text{Cp}^*\text{IrW}_3\text{O}_{12}(\text{OH})\}^{5-}$ cubes into a $[\{\text{Cp}^*\text{IrW}_3\text{O}_{12}(\text{OH})\}_2\{\text{cis-Fe}(\text{OH}_2)_2\}_2]^{4-}$ core; the other two are dangling $\{\text{Fe}(\text{OH}_2)_4\}^{3+}$ cations (Fe2, O16, O17, O18, and O19) that bind to the peripheral sites of the $[(\text{Cp}^*\text{Ir})_2\text{W}_6\text{Fe}_2\text{O}_{24}(\text{OH})_2(\text{OH}_2)_4]^{4-}$ core, giving $[\{\text{Fe}(\text{OH}_2)_4\}_2\{\text{Cp}^*\text{IrW}_3\text{O}_{12}(\text{OH})\}_2\{\text{cis-}$

1
2
3
4 $\text{Fe}(\text{OH}_2)_2\}_2]^{2+}$. As such, the cationic organo-POM of **3-Fe** can be viewed as derived from Ir_4W_8
5
6
7 in which the *cis*- $\{\text{WO}_2\}^{2+}$ and dangling $\{\text{Cp}^*\text{Ir}(\text{OH}_2)\}^{2+}$ are totally replaced by *cis*- $\{\text{Fe}(\text{OH}_2)_2\}^{3+}$
8
9
10 and $\{\text{Fe}(\text{OH}_2)_4\}^{3+}$. This substitution changes the distance between the $\{\text{Cp}^*\text{IrW}_3\text{O}_{12}(\text{OH})\}^{5-}$
11
12
13 units (see Figure S8 for the comparison of this distance in all compounds). The *cis*- $\{\text{MO}_2\}^{2+}$ is a
14
15
16
17 common building unit in polyoxometalate structures and is often found as a linker in
18
19
20 polyoxometalate dimers^{42, 43}. In addition, Pope et al. reported that *cis*- $\{\text{MoO}_2\}^{2+}$ and *cis*-
21
22
23 $\{\text{Co}(\text{ethylenediamine})\}^{3+}$ are topologically identical, and hence the latter easily fused into the
24
25
26
27 framework of a polyoxomolybdate.⁴⁴
28
29
30
31
32
33
34
35
36
37
38
39
40
41
42
43
44
45
46
47
48
49
50
51
52
53
54
55
56
57
58
59
60

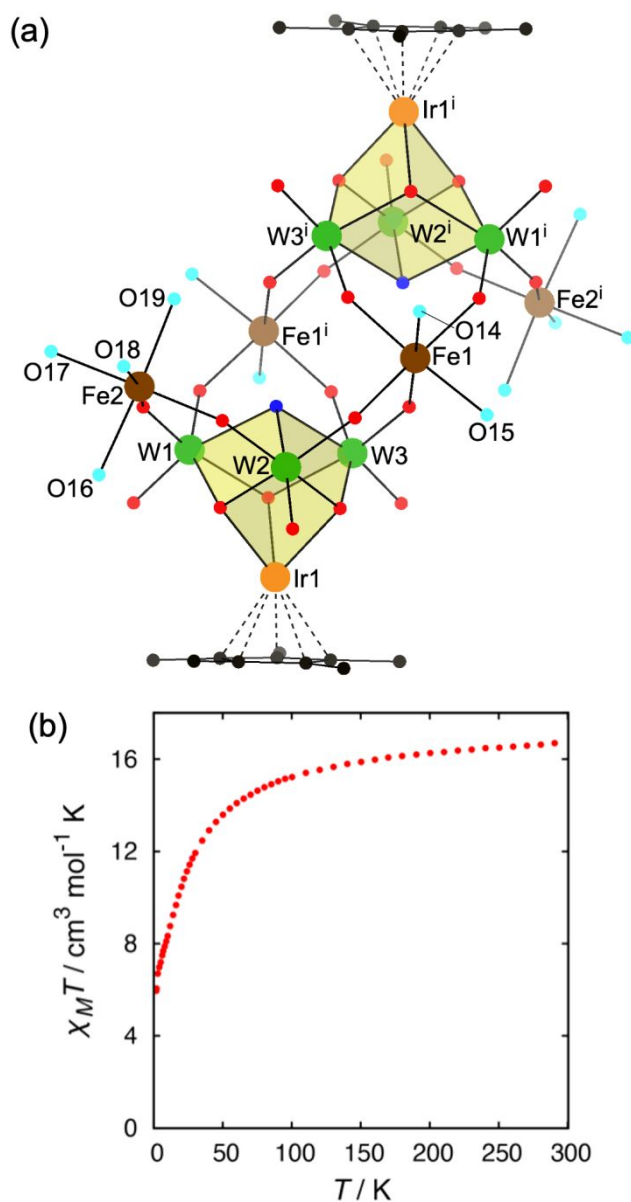


Figure 4. (a) Structure of the cationic part of **3-Fe** and (b) the $\chi_M T$ versus T plot of **3-Fe**. Color scheme: green, W; orange, Ir; brown, Fe; red, O; blue, protonated O (OH^-); cyan, O of aquo ligands; black, C. The hydrogen atoms are omitted for clarity. Symmetry operation: (i) $-x, -y, -z$.

The Fe1...Fe1 and Fe1...Fe2 separations in **3-Fe** are 5.428 and 5.903 Å, respectively. As a comparison, the M1...M1 separations in **3-Cr** and **3-In** are 5.53 and 5.59 Å, respectively; the M1...M2 separations are 5.93 Å in **3-Cr** and 6.09 Å in **3-In**. BVS calculations confirmed that all the iron and tungsten atoms in **3-Fe** have +3 and +6 oxidation states, respectively, and all oxygen atoms (O14 to O19) bound to iron(III) are water molecules. SQUID magnetochemical analyses found the molar magnetic susceptibility ($\chi_m T$) of **3-Fe** at 300 K is 16.7 cm³ mol⁻¹ K, which is close to the theoretical value for four high-spin Fe³⁺ centers ($\chi_m T$ spin-only = 17.54 cm³ mol⁻¹ K, assuming $g = 2.0$); the $\chi_m T$ further decreases on cooling, which is indicative of anti-ferromagnetic exchange interactions among the iron centers (Figure 4b). The magnetization under an external magnetic field of 5 T is 8.5 $N\mu_B$, which has not reached saturation (Figure S9). As such, the magnetic property of **3-Fe** is comparable to that of the Krebs-type tetrairon(III)-polyoxotungstate [Fe₄(OH₂)₁₀{ β -AsW₉O₃₄}₂]⁶⁻.⁴⁵

Water-oxidation properties

Recently, water-insoluble polyoxometalate compounds, particularly those containing cobalt, have gained interest as solid heterogeneous water oxidation catalysts.^{26, 46, 47} All of our compounds are insoluble in water, and hence we investigated their water-oxidation properties

1
2
3
4 using a carbon paste electrode technique. Figure 5a shows linear sweep voltammograms of the
5
6
7 carbon paste mixture of **1**, **2-Co**, or **3-Fe** in comparison with the voltammograms of the pure
8
9
10 carbon paste and carbon paste mixture of $[(\text{Cp}^*\text{IrCl})_2(\mu\text{-Cl})_2]$. The concentration of the analyte in
11
12
13 the carbon paste mixture was 10 wt%. All compounds show a water oxidation current, with **3-Fe**
14
15
16 being the least active. The catalytic current of **1** is most likely caused by iridium species
17
18
19 generated from the oxidation of the dangling $\{\text{Cp}^*\text{Ir}(\text{OH}_2)\}^{2+}$ units,⁴⁸ as evidenced by the
20
21
22
23 shoulder around +1.1 V in the voltammogram. Since a similar shoulder is not observed in **2-Co**
24
25
26 and **3-Fe**, the $\{\text{Cp}^*\text{Ir}\}^{2+}$ fragment of the $\{\text{Cp}^*\text{IrW}_3\text{O}_{12}(\text{OH})\}^{5-}$ building blocks might be less
27
28
29 contributing to the electrocatalytic water oxidation, and the activity of **2-Co** is due to the cobalt
30
31
32
33 ions.
34
35
36
37
38
39
40
41
42
43
44
45
46
47
48
49
50
51
52
53
54
55
56
57
58
59
60

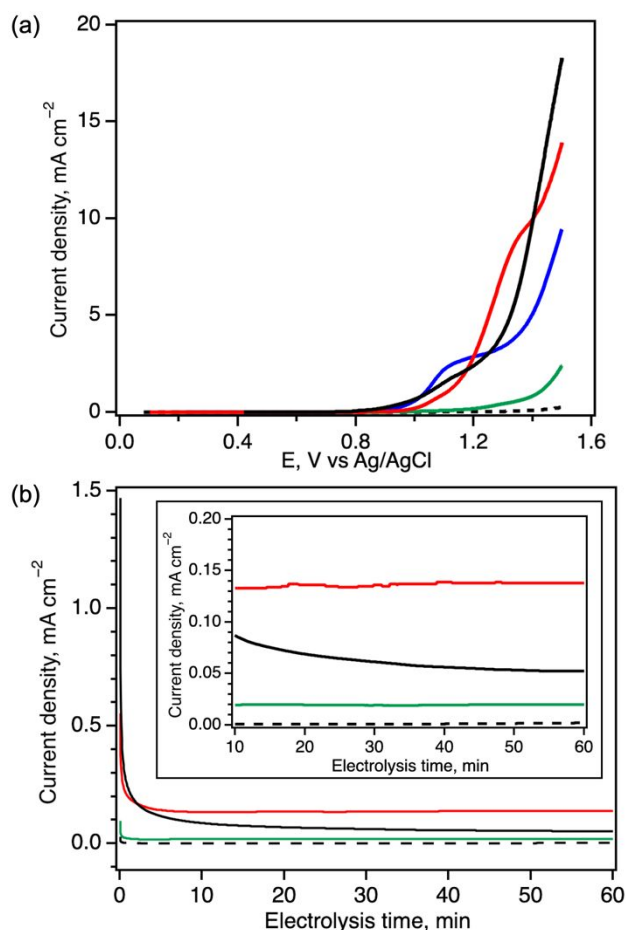


Figure 5. (a) Solid-state linear sweep voltammograms and (b) current–time plot showing current generated over 1 h of controlled-potential electrolysis, with the inset showing an enlarged view of the plot for the electrolysis time period of 10–60 min. Color scheme: **1** (black trace), **2-Co** (red trace), **3-Fe** (green trace), carbon paste (dashed black trace), and [(Cp*IrCl)₂(μ-Cl)₂] (blue trace).

Controlled potential electrolysis (with an applied potential of +1.1 V vs. Ag/AgCl) of the carbon paste mixtures of **1**, **2-Co**, or **3-Fe** in 0.05 M sodium phosphate buffer (pH 7) showed that **2-Co** gives the highest current density of 0.13–0.14 mA/cm², which is maintained for 1 h and a

short incubation time (less than 10 min), as shown in Figure 5b. The total cobalt concentration in the 10 wt% **2-Co**/carbon paste mixture is approximately 0.6 wt%. As a comparison, the 44 wt% $\text{Cs}_8\text{K}[\text{Co}_9(\text{H}_2\text{O})_6(\text{OH})_3(\text{HPO}_4)_2(\text{PW}_9\text{O}_{34})_3]\cdot 41\text{H}_2\text{O}$ /carbon paste mixture has a total cobalt concentration of 2.26 wt% and generates a current density of approximately 0.42 mA/cm^2 .²⁶ Increasing the concentration of **2-Co** to 30% increases the current density to approximately 0.5 mA/cm^2 , which is similar to the current density generated by the 10 wt% (approximately 6.3 wt% total cobalt concentration) of cobalt(II) hydroxide/carbon paste mixture (Figure S10). As such, **2-Co** could generate considerable current at a lower cobalt content. The PXRD patterns of the carbon-paste mixtures before and after electrolysis were similar (Figure S11), and the FTIR spectra of the recovered **2-Co** and **3-Fe** after electrolysis did not show significant changes (Figure S12). Although these characterizations are insufficient to identify the true catalysts, **2-Co** is a potential precursor for water oxidation catalysts.

Conclusion

We have successfully introduced metal-aquo complexes of silver(I), cobalt(II)/nickel(II), and iron(III)/chromium(III)/indium(III) on the framework of Cp^*Ir -polyoxotungstates through substitution of Cp^*Ir fragments and/or *cis*- $\{\text{WO}_2\}^{2+}$ units. Each transition-metal cation reacted

1
2
3
4 distinctively with the Cp*Ir-octatungstate clusters. The softer silver(I) cations prefer the binding
5
6
7 sites close to the Cp* ligands to gain stabilization through Ag...H₃C contacts. The dicationic
8
9
10 {Co(OH₂)₂}²⁺ ions exhibit both *trans* and *cis* isomers, with the *trans* isomers serving as linkers
11
12
13 that facilitate the formation of one-dimensional chains of organoiridium-tungsten-cobalt oxides.
14
15
16 Moreover, *cis*-{Co(OH₂)₂}²⁺ and *cis*-{Fe(OH₂)₂}³⁺ fragments could replace the *cis*-{WO₂}²⁺
17
18
19 units, suggesting that *cis*-{M(OH₂)₂}^{*n*+} metal-aquo cations are topological analogues of *cis*-
20
21
22 {WO₂}²⁺ or *cis*-{MoO₂}²⁺ units. The cobalt(II)-incorporated Cp*Ir-polyoxotungstate showed the
23
24
25 best water-oxidation activity. These compounds are molecular models for a catalytic active
26
27
28 center on complex oxides. As such, substitution reaction of labile organometallic groups of an
29
30
31 organometallic-polyoxometalate allows precise incorporation of coordination complexes in the
32
33
34 target sites and hence is a powerful method to install new functionality in complex metal oxide
35
36
37 clusters.
38
39
40
41
42
43
44
45
46
47
48

49 ASSOCIATED CONTENT
50
51
52
53
54
55
56
57
58
59
60

Supporting Information. Additional experimental results, Crystallographic parameters, BVS results (PDF).

Accession Codes. CCDC 2171548 (**1**), 2180597 (**2-Co**), 2321602 (**2-Ni**), 2321600 (**3-Cr**), 2222174 (**3-Fe**), and 2321601 (**3-In**) contain the supplementary crystallographic data for this paper. These data can be obtained free of charge via www.ccdc.cam.ac.uk/data_request/cif, or by emailing data_request@ccdc.ca.ac.uk, or by contacting The Cambridge Crystallographic Data Centre, 12 Union Road, Cambridge CB2 1EZ, UK; fax: +44 1223 336033.

AUTHOR INFORMATION

Corresponding Author

*Email: sadakane09@hiroshima-u.ac.jp

Author Contributions

R.M. collected and analyzed the SQUID magnetic susceptibility data. The manuscript was written through the contributions of all authors. All authors have given their approval to the final version of the manuscript.

Funding Sources

The New Energy and Industrial Technology and Development Organization (NEDO) of Japan (Project JPNP20005). JSPS KAKENHI Grant-in-Aid for Transformative Research Area (A) “Supra-ceramics” (JP22H05144), JSPS Core-to-Core program, and International Network on Polyoxometalate Science at Hiroshima University. ARIM of the MEXT (Project JPMXP1223MS1015).

Notes

The authors declare no competing financial interests.

ACKNOWLEDGMENT

This study was commissioned by the New Energy and Industrial Technology and Development Organization (NEDO) of Japan (Project JPNP20005). We acknowledge support from the JSPS KAKENHI Grant-in-Aid for Transformative Research Area (A) “Supra-ceramics” (JP22H05144), the JSPS Core-to-Core program, and the International Network on Polyoxometalate Science at Hiroshima University. The magnetic measurements were conducted at the Institute of Molecular Science, supported by ARIM of the MEXT (Project JPMXP1223MS1015). We acknowledge Ms.

M. Kosaka and Mr. M. Kobayashi at the Division of Instrumental Analysis in Okayama for performing CHN elemental analyses.

ABBREVIATIONS

POM, polyoxometalate; organo-POM, organometallic-polyoxometalate; FTIR, Fourier transform infrared; PXRD, powder X-ray diffraction; TGA thermogravimetric analyses.

REFERENCES

(1) Misra, A.; Kozma, K.; Streb, C.; Nyman, M. Beyond Charge Balance: Counter-Cations in Polyoxometalate Chemistry. *Angew. Chem. Int. Ed.* **2020**, *59* (2), 596-612. DOI: 10.1002/anie.201905600.

(2) Gumerova, N. I.; Rompel, A. Polyoxometalates in solution: speciation under spotlight. *Chem. Soc. Rev.* **2020**, *49* (21), 7568-7601. DOI: 10.1039/d0cs00392a.

(3) Liu, Z.-J.; Wang, X.-L.; Qin, C.; Zhang, Z.-M.; Li, Y.-G.; Chen, W.-L.; Wang, E.-B. Polyoxometalate-assisted synthesis of transition-metal cubane clusters as artificial mimics of the

oxygen-evolving center of photosystem II. *Coord. Chem. Rev.* **2016**, *313*, 94-110. DOI: 10.1016/j.ccr.2015.12.006.

(4) Niu, J.; Yang, L.; Zhao, J.; Ma, P.; Wang, J. Novel octatungstate-supported tricarbonyl metal derivatives: $\{[H_2W_8O_{30}][M(CO)_3]_2\}^{8-}$ (M = Mn(I) and Re(I)). *Dalton Trans.* **2011**, *40*(33), 8298-8300. DOI: 10.1039/c1dt11042j.

(5) Zhang, D.; Zhao, J.; Zhang, Y.; Hu, X.; Li, L.; Ma, P.; Wang, J.; Niu, J. Octamolybdate-supported tricarbonyl metal derivatives: $\{[H_2Mo_8O_{30}]\{M(CO)_3\}_2\}^{8-}$ (M = Mn(I) and Re(I)). *Dalton Trans* **2013**, *42* (8), 2696-2699. DOI: 10.1039/c2dt32678g.

(6) Süss-Fink, G.; Plasseraud, L.; Ferrand, V.; Stoeckli-Evans, H. $[(p\text{-Pr}^iC_6H_4Me)_4Ru_4Mo_4O_{16}]$: an amphiphilic organoruthenium oxomolybdenum cluster presenting a unique framework geometry. *Chem. Commun.* **1997**, (17), 1657-1658. DOI: 10.1039/a703035e.

(7) Artero, V.; Proust, A.; Herson, P.; Gouzerh, P. Interplay of Cubic Building Blocks in $(\eta^6\text{-arene})\text{Ruthenium-Containing Tungsten and Molybdenum Oxides}$. *Chem. – Eur. J.* **2001**, *7*(18), 3901-3910. DOI: 10.1002/1521-3765(20010917)7:18<3901::Aid-chem3901>3.0.Co;2-3.

(8) Hayashi, Y.; Müller, F.; Lin, Y.; Miller, S. M.; Anderson, O. P.; Finke, R. G. $2\text{CH}_3\text{CN} \subset (n\text{-Bu}_4\text{N})_2[\{\text{Ir}(1,5\text{-COD})\}_6\text{W}_4\text{O}_{16}]\cdot 2\text{CH}_3\text{CN}$: A Hybrid Inorganic–Organometallic, Flexible Cavity Host, Acetonitrile–Guest Complex Composed of a $[\text{W}_4\text{O}_4]^{n+}$ Tetrahedron Cube and Six Polyoxoanion-Supported (1,5-COD) Ir^+ Organometallic Groups. *J. Am. Chem. Soc.* **1997**, *119* (47), 11401-11407. DOI: 10.1021/ja970336h.

(9) Putaj, P.; Lefebvre, F. Polyoxometalates containing late transition and noble metal atoms. *Coord. Chem. Rev.* **2011**, *255* (15-16), 1642-1685. DOI: 10.1016/j.ccr.2011.01.030.

(10) Isobe, K.; Yagasaki, A. Cubane-type clusters as potential models for inorganic solid surfaces. *Acc. Chem. Res.* **1993**, *26* (10), 524-529. DOI: 10.1021/ar00034a002.

(11) Hayashi, S.; Shishido, T. High-Density Formation of Metal/Oxide Interfacial Catalytic Active Sites through Hybrid Clustering. *ACS Appl. Mater. Interfaces* **2021**, *13* (19), 22332-22340. DOI: 10.1021/acsami.1c02240.

(12) Hayashi, S.; Endo, S.; Miura, H.; Shishido, T. Highly Active and Durable Rh–Mo-Based Catalyst for the $\text{NO-CO-C}_3\text{H}_6\text{-O}_2$ Reaction Prepared by Using Hybrid Clustering. *ACS Materials Au* **2023**, *3* (5), 456-463. DOI: 10.1021/acsmaterialsau.3c00001.

(13) Hayashi, S.; Shishido, T. High-Density Formation of Ir/MoO(x) Interface through Hybrid Clustering for Chemoselective Nitrostyrene Hydrogenation. *ACS Org Inorg Au* **2023**, *3* (5), 283-290. DOI: 10.1021/acsorginorgau.3c00017.

(14) Laurencin, D.; Garcia Fidalgo, E.; Villanneau, R.; Villain, F.; Herson, P.; Pacifico, J.; Stoeckli-Evans, H.; Benard, M.; Rohmer, M. M.; Suss-Fink, G.; et al. Framework fluxionality of organometallic oxides: synthesis, crystal structure, EXAFS, and DFT studies on [[Ru(η^6 -arene)]₄Mo₄O₁₆] complexes. *Chem. – Eur. J.* **2004**, *10* (1), 208-217. DOI: 10.1002/chem.200305396.

(15) Laurencin, D.; Villanneau, R.; Proust, A.; Brethon, A.; Arends, I. W. C. E.; Sheldon, R. A. Relationship between structure, fluxionality and racemization activity in organometallic derivatives of polyoxometalates. *Tetrahedron: Asymmetry* **2007**, *18* (3), 367-371. DOI: 10.1016/j.tetasy.2007.02.002.

(16) Laurencin, D.; Thouvenot, R.; Boubekur, K.; Villain, F.; Villanneau, R.; Rohmer, M.-M.; Bénard, M.; Proust, A. Experimental and Computational Study of the Framework Fluxionality of

Organometallic Derivatives of Polyoxometalates: Analysis of the Effect of the Metal and of the Solvent. *Organometallics* **2009**, *28*(11), 3140-3151. DOI: 10.1021/om8011568.

(17) Besecker, C. J.; Day, V. W.; Klemperer, W. G.; Thompson, M. R. [(Me₅C₅)Rh(*cis*-Nb₂W₄O₁₉)]²⁻ isomers: synthesis, structure, and dynamics. *J. Am. Chem. Soc.* **1984**, *106* (15), 4125-4136. DOI: 10.1021/ja00327a011.

(18) Abe, M.; Isobe, K.; Kida, K.; Yagasaki, A. Crystallographic and Dynamic NMR Evidence for Organometallic Fragments Pivoting on a Molecular Oxide Surface. *Inorg. Chem.* **1996**, *35* (18), 5114-5115. DOI: 10.1021/ic960297v.

(19) Nishikawa, K.; Kido, K.; Yoshida, J. i.; Nishioka, T.; Kinoshita, I.; Breedlove, B. K.; Hayashi, Y.; Uehara, A.; Isobe, K. Synthesis and behavior in solution of the triple cubane- and windmill-type framework isomers of an organorhodium tungsten oxide cluster [(Cp*Rh)₄W₄O₁₆]. *Appl. Organomet. Chem.* **2003**, *17*(6-7), 446-448. DOI: 10.1002/aoc.447.

(20) Mukhacheva, A. A.; Volcheck, V. V.; Sheven, D. G.; Yanshole, V. V.; Kompankov, N. B.; Haouas, M.; Abramov, P. A.; Sokolov, M. N. Coordination capacity of Keggin anions as polytopic

ligands: case study of $[\text{VNb}_{12}\text{O}_{40}]^{15-}$. *Dalton Trans.* **2021**, *50* (20), 7078-7084. DOI: 10.1039/d1dt00765c.

(21) Hayashi, Y.; Ozawa, Y.; Isobe, K. Site-selective oxygen exchange and substitution of organometallic groups in an amphiphilic quadruple-cubane-type cluster. Synthesis and molecular structure of $[(\text{MCp}^*)_4\text{V}_6\text{O}_{19}]$ (M = rhodium, iridium). *Inorg. Chem.* **1991**, *30*(5), 1025-1033. DOI: 10.1021/ic00005a028.

(22) Sugiarto; Tagami, T.; Kawamoto, K.; Hayashi, Y. Synthesis of cationic molybdenum-cobalt heterometallic clusters protected against hydrolysis by macrocyclic triazacyclononane complexes. *Dalton Trans.* **2018**, *47*(29), 9657-9664. DOI: 10.1039/c8dt01226a.

(23) Sugiarto; Imai, Y.; Hayashi, Y. Synthesis of Water-Soluble Planar Cobalt(II), Nickel(II), and Copper(II) Hydroxo Clusters Using a (1,4,7-Triazacyclononane)cobalt(III) Complex as a Hydrolysis-Terminating Group. *Inorg. Chem.* **2023**, *62* (5), 1845-1854. DOI: 10.1021/acs.inorgchem.2c01046.

(24) Kastner, K.; Margraf, J. T.; Clark, T.; Streb, C. A molecular placeholder strategy to access a family of transition-metal-functionalized vanadium oxide clusters. *Chem. – Eur. J.* **2014**, *20*(38), 12269-12273. DOI: 10.1002/chem.201403592.

(25) Sugiarto; Shinogi, J.; Sadakane, M. Molar-Ratio-Dependent Coordination Assembly of Organoiridium(III)-Octatungstate Complexes in Aqueous Solution. *Inorg. Chem.* **2023**, *62* (17), 6759-6767. DOI: 10.1021/acs.inorgchem.3c00479.

(26) Soriano-Lopez, J.; Goberna-Ferron, S.; Vigarra, L.; Carbo, J. J.; Poblet, J. M.; Galan-Mascaros, J. R. Cobalt polyoxometalates as heterogeneous water oxidation catalysts. *Inorg. Chem.* **2013**, *52* (9), 4753-4755. DOI: 10.1021/ic4001945.

(27) Bruker. *APEX3, SADABS, SAINT* 2016.

(28) Sheldrick, G. M. SHELXT - integrated space-group and crystal-structure determination. *Acta Crystallogr., Sect. A: Found. Adv.* **2015**, *71* (Pt 1), 3-8. DOI: 10.1107/S2053273314026370.

(29) Sheldrick, G. M. Crystal structure refinement with SHELXL. *Acta Crystallogr., Sect. C: Struct. Chem.* **2015**, *71* (Pt 1), 3-8. DOI: 10.1107/S2053229614024218.

(30) Hubschle, C. B.; Sheldrick, G. M.; Dittrich, B. ShelXle: a Qt graphical user interface for SHELXL. *J. Appl. Crystallogr.* **2011**, *44* (Pt 6), 1281-1284. DOI: 10.1107/S0021889811043202.

(31) Spek, A. L. PLATON SQUEEZE: a tool for the calculation of the disordered solvent contribution to the calculated structure factors. *Acta Crystallogr., Sect. C: Struct. Chem.* **2015**, *71* (Pt 1), 9-18. DOI: 10.1107/S2053229614024929.

(32) Brese, N. E.; O'Keeffe, M. Bond-valence parameters for solids. *Acta Crystallogr. Sect. B: Struct. Sci.* **1991**, *47*(2), 192-197. DOI: 10.1107/s0108768190011041.

(33) Singh, V.; Ma, P.; Drew, M. G. B.; Wang, J.; Niu, J. A comprehensive approach providing a new synthetic route for bimetallic electrocatalysts via isoPOMs [M/Rh(Cp*)₄W₈O₃₂] (M = Rh (1) and Ir (2)). *Dalton Trans.* **2018**, *47*(39), 13870-13879. DOI: 10.1039/c8dt03227k.

(34) Ingleson, M. J.; Mahon, M. F.; Patmore, N. J.; Ruggiero, G. D.; Weller, A. S. [(PPh₃)Ag(HCB₁₁)Me₁₁]: a complex with intermolecular Ag...H₃C interactions. *Angew. Chem. Int. Ed.* **2002**, *41* (19), 3694-3697; 3522. DOI: 10.1002/1521-3773(20021004)41:19<3694::AID-ANIE3694>3.0.CO;2-B.

(35) Liu, C.-S.; Chen, P.-Q.; Chang, Z.; Wang, J.-J.; Yan, L.-F.; Sun, H.-W.; Bu, X.-H.; Lin, Z.; Li, Z.-M.; Batten, S. R. A photoluminescent hexanuclear silver(I) complex exhibiting C–H···Ag close interactions. *Inorg. Chem. Commun.* **2008**, *11* (2), 159-163. DOI: 10.1016/j.inoche.2007.11.014.

(36) Ilie, A.; Rat, C. I.; Scheutzw, S.; Kiske, C.; Lux, K.; Klapotke, T. M.; Silvestru, C.; Karaghiosoff, K. Metallophilic bonding and agostic interactions in gold(I) and silver(I) complexes bearing a thiotetrazole unit. *Inorg. Chem.* **2011**, *50* (6), 2675-2684. DOI: 10.1021/ic102595d.

(37) Abramov, P. A. Study of the structure of Ag(I) solvate complexes by means of polyoxometalates: crystallization from the AgNO₃/(Bu₄N)₄[β-Mo₈O₂₆]/DMF system. Review. *J. Struct. Chem.* **2022**, *63* (12), 2068-2082. DOI: 10.1134/s0022476622120186.

(38) Persson, I.; Nilsson, K. B. Coordination chemistry of the solvated silver(I) ion in the oxygen donor solvents water, dimethyl sulfoxide, and *N,N*-dimethylpropyleneurea. *Inorg. Chem.* **2006**, *45* (18), 7428-7434. DOI: 10.1021/ic060636c.

(39) Surinwong, S.; Yoshinari, N.; Yotnoi, B.; Konno, T. An Extremely Porous Hydrogen-Bonded Framework Composed of D-Penicillaminato Co^{III}₂Au^I₃ Complex Anions and Aqua

Cobalt(II) Cations: Formation and Stepwise Structural Transformation. *Chem. Asian J.* **2016**, *11* (4), 486-490. DOI: 10.1002/asia.201501352.

(40) Mukhacheva, A. A.; Komarov, V. Y.; Kokovkin, V. V.; Novikov, A. S.; Abramov, P. A.; Sokolov, M. N. Unusual π - π interactions directed by the $[(C_6H_6)Ru_2W_8O_{30}(OH)_2]^{6-}$ hybrid anion. *CrystEngComm* **2021**, *23* (23), 4125-4135. DOI: 10.1039/d1ce00319d.

(41) Helm, L.; Merbach, A. E. Inorganic and bioinorganic solvent exchange mechanisms. *Chem Rev* **2005**, *105* (6), 1923-1959. DOI: 10.1021/cr030726o.

(42) Nomiya, K.; Hayashi, K.; Kasahara, Y.; Iida, T.; Nagaoka, Y.; Yamamoto, H.; Ueno, T.; Sakai, Y. Organometallic Complexes Supported on a Metal-Oxide Cluster. pH-Dependent Interconversion between the Monomeric and Dimeric Species of the Polyoxoanion-Supported $[(arene)Ru]^{2+}$ Complex. *Bull. Chem. Soc. Jpn.* **2007**, *80* (4), 724-731. DOI: 10.1246/bcsj.80.724.

(43) Artero, V.; Laurencin, D.; Villanneau, R.; Thouvenot, R.; Herson, P.; Gouzerh, P.; Proust, A. Synthesis, characterization, and photochemical behavior of $\{Ru(arene)\}^{2+}$ derivatives of alpha- $[PW_{11}O_{39}]^{7-}$: an organometallic way to ruthenium-substituted heteropolytungstates. *Inorg. Chem.* **2005**, *44* (8), 2826-2835. DOI: 10.1021/ic0482180.

(44) Belai, N.; Kapoor, P. N.; Dickman, M. H.; Butcher, R. J.; Pope, M. T. Fusion of Coordination - and Polyoxometalate Chemistry - Chelated Cobalt(III) Centers as Structural Components of Polyoxomolybdates - $[\{\text{Co}(\text{en})\}_4\text{Mo}_{10}\text{O}_{38}]^{4-}$ and Macrocyclic $[\{\text{Co}^{\text{II}}(\text{H}_2\text{O})_2\} - \{\text{Co}(\text{en})\}_8\{\text{Mo}_{20}\text{O}_{76}\}]^{6-}$. *Eur. J. Inorg. Chem.* **2009**, 2009 (34), 5215-5218. DOI: 10.1002/ejic.200900599.

(45) Prinz, M.; Takács, A. F.; Schnack, J.; Balasz, I.; Burzo, E.; Kortz, U.; Kuepper, K.; Neumann, M. Magnetic and electronic properties of the iron-containing polyoxotungstate $[\text{Fe}_4(\text{H}_2\text{O})_{10}(\beta\text{-SbW}_9\text{O}_{33})_2]^{6-}$. *J. Appl. Phys.* **2006**, 99(8). DOI: 10.1063/1.2173613.

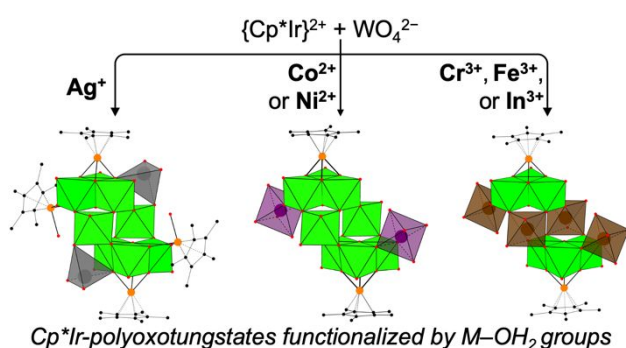
(46) Hu, Q.; Chen, S.; Wagberg, T.; Zhou, H.; Li, S.; Li, Y.; Tan, Y.; Hu, W.; Ding, Y.; Han, X. Developing Insoluble Polyoxometalate Clusters to Bridge Homogeneous and Heterogeneous Water Oxidation Photocatalysis. *Angew. Chem. Int. Ed.* **2023**, 62 (32), e202303290. DOI: 10.1002/anie.202303290.

(47) Blasco-Ahicart, M.; Soriano-Lopez, J.; Carbo, J. J.; Poblet, J. M.; Galan-Mascaros, J. R. Polyoxometalate electrocatalysts based on earth-abundant metals for efficient water oxidation in acidic media. *Nat. Chem.* **2018**, 10(1), 24-30. DOI: 10.1038/nchem.2874.

(48) Blakemore, J. D.; Schley, N. D.; Olack, G. W.; Incarvito, C. D.; Brudvig, G. W.; Crabtree, R. H. Anodic deposition of a robust iridium-based water-oxidation catalyst from organometallic precursors. *Chem. Sci.* **2011**, *2* (1), 94-98. DOI: 10.1039/c0sc00418a.

SYNOPSIS. We report on the reactivity of organoiridium-polyoxotungstate complexes with silver(I), cobalt(II), nickel(II), chromium(III), iron(III), and indium(III) aquo cations. The reaction produces a family of organoiridium-polyoxometalates functionalized by metal-aquo cations, and the cobalt-containing cluster exhibits the highest water oxidation activity. This study shows the potential of organometallic-polyoxometalate complexes as new building blocks for synthesizing multimetallic oxide clusters.

Graphical abstract (4.45 x 8.25)



Supporting Information

Reactivity of organoiridium tungsten oxide clusters with transition metal aquo cations

Sugiarto,^a Ryoji Mitsuhashi,^b and Masahiro Sadakane^{a}*

^aDepartment of Applied Chemistry, Graduate School of Advanced Science and Engineering, Hiroshima University, 1-4-1 Kagamiyama, Higashi-Hiroshima 739-8527, Japan

^bInstitute of Liberal Arts and Science, Kanazawa University, Kakuma, Kanazawa 920-1192, Japan

*Email: sadakane09@hiroshima-u.ac.jp

Contents

Table S1. Crystallographic parameters	S2
Table S2. Bond valence sum (BVS) calculation results	S3
Figure S1. Thermogram of 1	S4
Figure S2. FTIR spectra of all compounds	S5
Figure S3. Thermograms of 2-Co	S6
Figure S4. Thermogram of 2-Ni	S7
Figure S5. Thermograms of 3-Cr , 3-Fe , and 3-In	S8
Figure S6. ¹ H NMR spectra of 1 and [(Cp*Ir)(μ-OH) ₃] ₂ (Ir ₄ W ₈)	S9
Figure S7. Powder X-ray diffraction patterns of 2-Co	S10
Figure S8. Plot of interlayer (<i>d</i>) and M···M (<i>w</i>) distances of all compounds	S11
Figure S9. Magnetization curve of 3-Fe	S12
Figure S10. Current–time plots of the 30 wt% of 2-Co /carbon-paste mixture	S13
Figure S11. PXRD patterns of the carbon-paste mixtures before and after electrolysis	S14
Figure S12. FTIR spectra of the recovered samples after electrolysis	S15

Table S1. Crystallographic parameters. * Note that formulas and formula weights are based on X-ray diffraction results.

	1	2-Co	2-Ni	3-Cr	3-Fe	3-In
Formula unit*	C ₄₀ H ₆₀ Ag ₂ Ir ₃₄ O ₅₈ W ₈	C ₁₀ H ₁₅ Co _{1.02} IrK _{0.4} O _{21.56} W _{3.63}	C ₂₀ Ir ₂ K ₂ Ni _{13.05} O _{60.6} W _{7.07}	C ₂₀ H ₃₀ Cr ₄ Ir ₂ N ₂ O ₆₂ W ₆	C ₂₀ H ₉₂ Fe ₄ Ir ₂ N ₂ O ₆₂ W ₆	C ₂₀ H ₅₆ In ₄ Ir ₂ N ₂ O ₆₂ W ₆
Formula weight* (g/mol)	3924.22	1415.89	3150.68	2985.96	3063.85	3263.44
Crystal system	Monoclinic	Orthorhombic	Monoclinic	Triclinic	Triclinic	Triclinic
Space group (number)	<i>P</i> 2 ₁ / <i>n</i> (14)	<i>Pmma</i> (51)	<i>P</i> 2/ <i>m</i> (10)	<i>P</i> $\bar{1}$ (2)	<i>P</i> $\bar{1}$ (2)	<i>P</i> $\bar{1}$ (2)
<i>a</i> , Å	12.502(2)	20.860(3)	11.2540(6)	10.0182(11)	10.1082(5)	10.2083(8)
<i>b</i> , Å	15.354(3)	11.007(2)	10.9231(6)	11.4398(12)	11.5221(6)	11.6884(9)
<i>c</i> , Å	22.186(4)	17.004(2)	17.0878(9)	16.4259(18)	16.4844(8)	16.4963(13)
α , °	90	90	90	105.299(1)	105.036(1)	102.320(1)
β , °	94.754(2)	90	103.893(1)	102.559(1)	102.645(1)	102.190(1)
γ , °	90	90	90	100.123(1)	100.202(1)	100.259(1)
<i>V</i> , Å ³	4244.2(13)	3904.2(9)	2039.13(19)	1717.2(3)	1752.57(15)	1797.6(2)
<i>Z</i>	2	4	1	1	1	1
D _{calc} (g/cm ³)	3.071	2.409	2.566	2.888	2.903	3.015
μ (mm ⁻¹)	17.582	14.581	14.051	14.584	14.499	14.611
Radiation	Mo K α	Mo K α	Mo K α	Mo K α	Mo K α	Mo K α
	(λ = 0.71073 Å)	(λ = 0.71073 Å)	(λ = 0.71073 Å)	(λ = 0.71073 Å)	(λ = 0.71073 Å)	(λ = 0.71073 Å)
Temperature (K)	123(2)	123(2)	123(2)	123(2)	123(2)	123(2)
F ₀₀₀	3516	2514	1405	1354	1424	1480
Θ range	1.615 to 25.443°	1.545 to 26.452°	1.864 to 27.511°	1.338 to 29.076°	1.944 to 27.557°	1.330 to 27.528°
Index ranges	-15 ≤ <i>h</i> ≤ 14 -17 ≤ <i>k</i> ≤ 18 -26 ≤ <i>l</i> ≤ 26	-25 ≤ <i>h</i> ≤ 14 -13 ≤ <i>k</i> ≤ 13 -21 ≤ <i>l</i> ≤ 20	-14 ≤ <i>h</i> ≤ 13 -14 ≤ <i>k</i> ≤ 14 -22 ≤ <i>l</i> ≤ 21	-13 ≤ <i>h</i> ≤ 13 -14 ≤ <i>k</i> ≤ 14 -21 ≤ <i>l</i> ≤ 21	-13 ≤ <i>h</i> ≤ 13 -14 ≤ <i>k</i> ≤ 14 -21 ≤ <i>l</i> ≤ 21	-13 ≤ <i>h</i> ≤ 13 -15 ≤ <i>k</i> ≤ 15 -21 ≤ <i>l</i> ≤ 21
No. of reflections collected	30797	20629	17910	15559	15430	21158
Unique reflections (<i>R</i> _{int})	7796 (0.0659)	4350 (0.0794)	4927 (0.0265)	8163 (0.0329)	7898 (0.0212)	8174 (0.0370)
Data/restraints/parameters	7796/543/515	4350/269/202	4350/40/255	8163/527/433	7898/131/562	8174/104/481
<i>R</i> indexes [<i>I</i> > 2 σ (<i>I</i>)]	<i>R</i> ₁ ^a = 0.0390 <i>wR</i> ₂ ^b = 0.0862	<i>R</i> ₁ = 0.0503 <i>wR</i> ₂ = 0.1237	<i>R</i> ₁ = 0.0357 <i>wR</i> ₂ = 0.0820	<i>R</i> ₁ = 0.0440 <i>wR</i> ₂ = 0.1097	<i>R</i> ₁ = 0.0226 <i>wR</i> ₂ = 0.0469	<i>R</i> ₁ = 0.0272 <i>wR</i> ₂ = 0.0547
<i>R</i> indexes (all data)	<i>R</i> ₁ = 0.0569 <i>wR</i> ₂ = 0.0931	<i>R</i> ₁ = 0.0703 <i>wR</i> ₂ = 0.1324	<i>R</i> ₁ = 0.0378 <i>wR</i> ₂ = 0.0827	<i>R</i> ₁ = 0.0576 <i>wR</i> ₂ = 0.1178	<i>R</i> ₁ = 0.0259 <i>wR</i> ₂ = 0.0481	<i>R</i> ₁ = 0.0332 <i>wR</i> ₂ = 0.0568
G.O.F	1.034	1.064	1.289	1.032	1.045	1.036
(Δ/σ) _{max}	0.001	0.001	0.002	0.001	0.002	0.002
$\Delta\rho_{\text{max/min}}$ (e Å ⁻³)	4.115/-3.334	2.392/-2.661	2.407/-1.692	5.659/-4.466	1.700/-1.786	1.114/-1.059
CCDC number	2171548	2180957	2321602	2321600	2222174	2321602

$$^a R_1 = \{\Sigma||F_o| - |F_c||\} / \{\Sigma|F_o|\}; \quad ^b wR_2 = [\Sigma w(F_o^2 - F_c^2) / \Sigma wF_o^2]^{1/2}$$

Table S2. BVS calculation results showing the oxidation state of tungsten atoms and the protonation state of oxygen atoms. Mono-protonated oxygen atoms (OH) are shown in red, whereas di-protonated oxygen atoms (H₂O) are shown in blue. *Note that the BVS values of atoms with asterisk marks are lower than the expected values because of the partial substitution of {WO₂} to {M(OH₂)}, hindering precise determination of the bond distances.

1		2-Co		2-Ni		3-Cr		3-Fe		3-In	
W1	6.00	W1	5.81	W1	5.87	W1	5.86	W1	5.81	W1	5.85
W2	5.53	W2	5.97	W2	5.81	W2	5.89	W2	5.83	W2	5.91
W3	5.99	W3*	5.12	W3*	4.98	W3	5.87	W3	5.84	W3	5.91
W4	5.92										
		Co1	2.01	Ni1	2.02	Cr1	3.02	Fe1	3.02	In1	3.22
Ag1	0.90					Cr2	3.12	Fe2	3.10	In2	3.28
		O1	1.80	O1	1.80						
O1	1.85	O2	1.65	O2	1.70	O1	1.52	O1	1.50	O1	1.60
O2	1.72	O3	1.83	O3	1.50	O2	1.80	O2	1.78	O2	1.90
O3	1.67	O4	1.66	O4	1.87	O3	1.59	O3	1.60	O3	1.77
O4	1.90	O5	1.20	O5	1.17	O4	1.72	O4	1.94	O4	1.71
O5	1.84	O6	1.65	O6	1.54	O5	1.77	O5	1.83	O5	1.74
O6	1.20	O7	1.76	O7	1.79	O6	1.57	O6	1.91	O6	1.04
O7	1.60	O8	2.00	O8	1.99	O7	1.71	O7	1.15	O7	1.62
O8	1.65	O9*	1.16	O9	0.29	O8	1.80	O8	1.75	O8	1.81
O9	1.98	O10	0.25	O10*	1.12	O9	1.73	O9	1.75	O9	1.95
O10	1.66	O11	0.36	O11	0.33	O10	1.19	O10	1.84	O10	1.80
O11	1.53			O12	0.32	O11	1.84	O11	1.60	O11	1.55
O12	1.90					O12	1.89	O12	1.75	O12	1.98
O13	1.95					O13	1.90	O13	1.71	O13	1.91
O14	1.60					O14	0.52	O14	0.42		
O15	1.85					O15	0.50	O15	0.47	OA1	0.51
O16	0.39					O16	0.52	O16	0.40	OA2	0.48
O17	0.25					O17	0.48	O17	0.47	OA3	0.44
O18	0.28					O18	0.49	O18	0.46	OA4	0.54
						O19	0.45	O19	0.52	OA5	0.52
										OA6	0.55

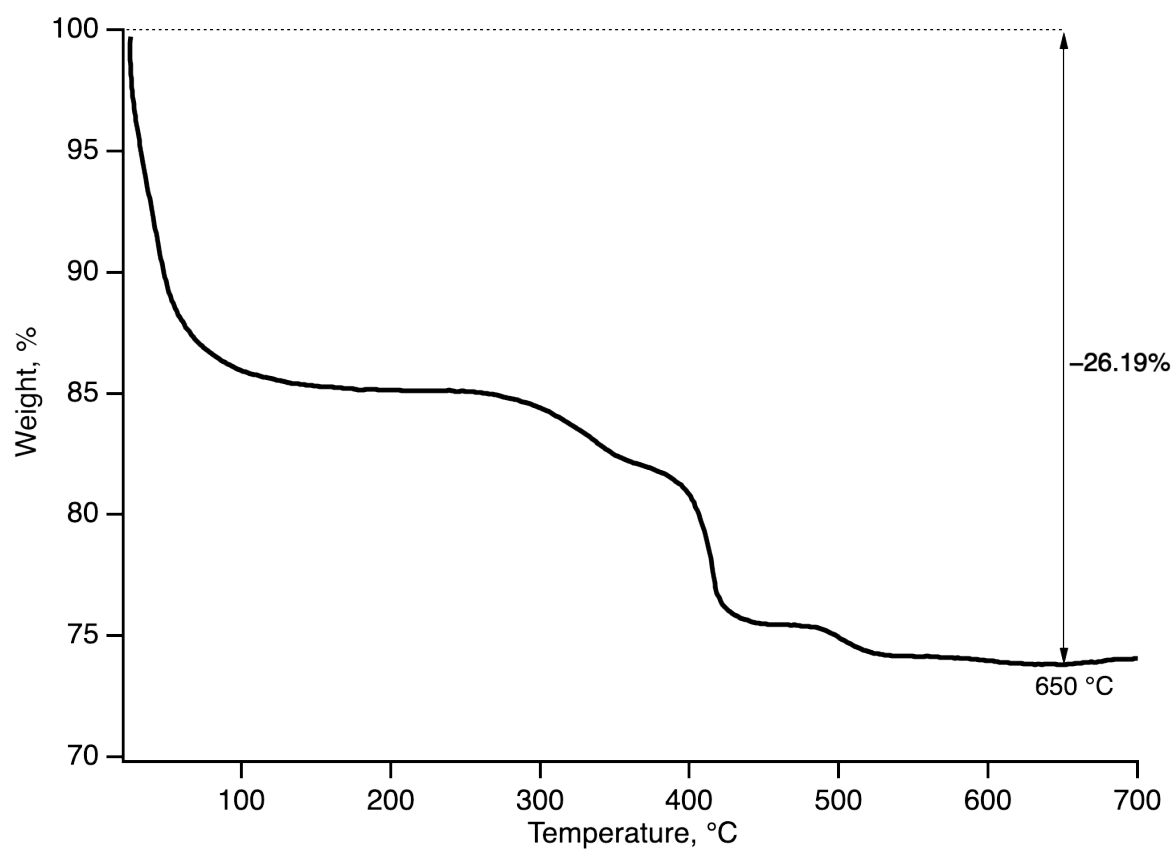


Figure S1. Thermogram of **1**.

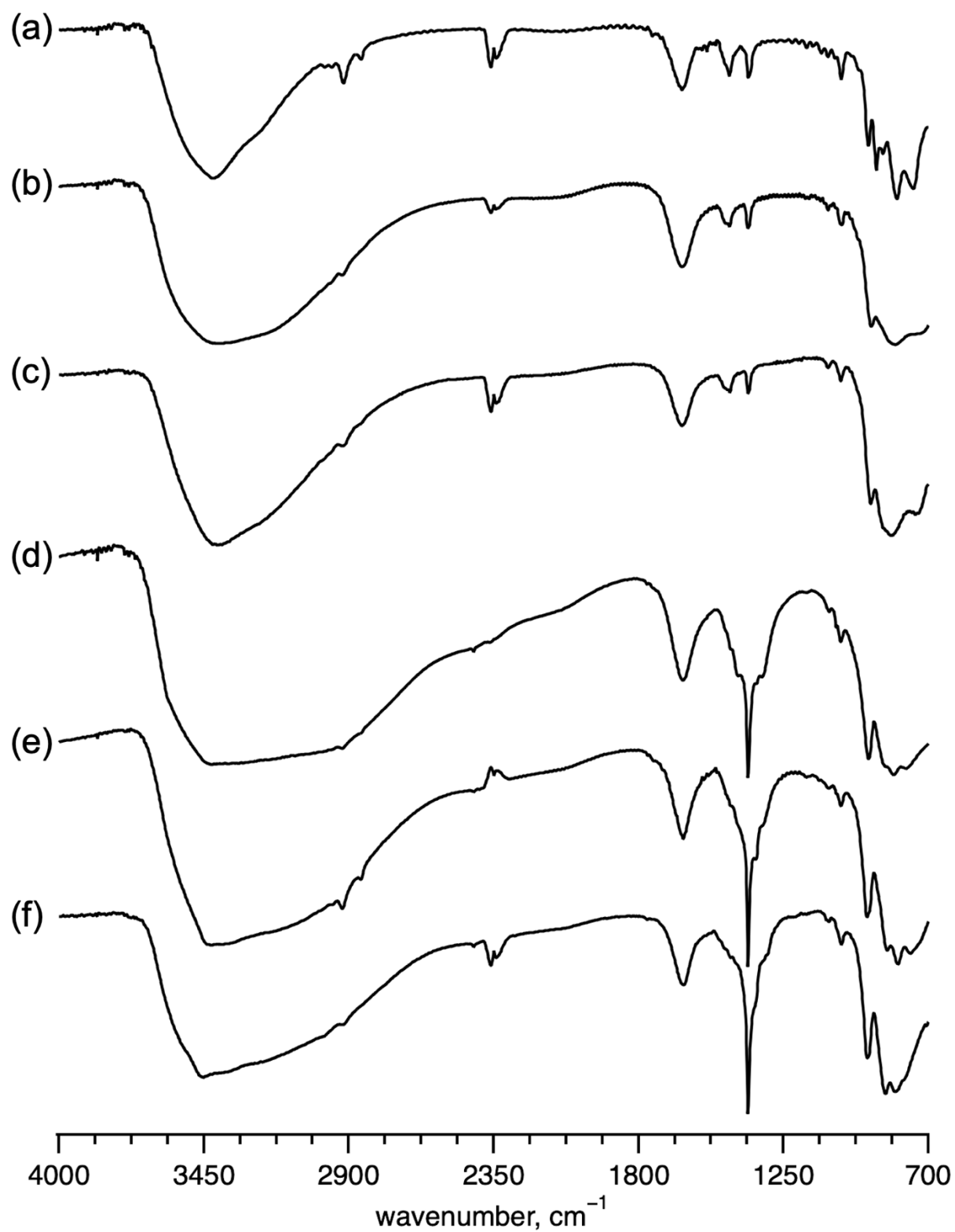


Figure S2. FTIR spectra of (a) **1**, (b) **2-Co**, (c) **2-Ni**, (d) **3-Cr**, (e) **3-Fe**, and (f) **3-In**.

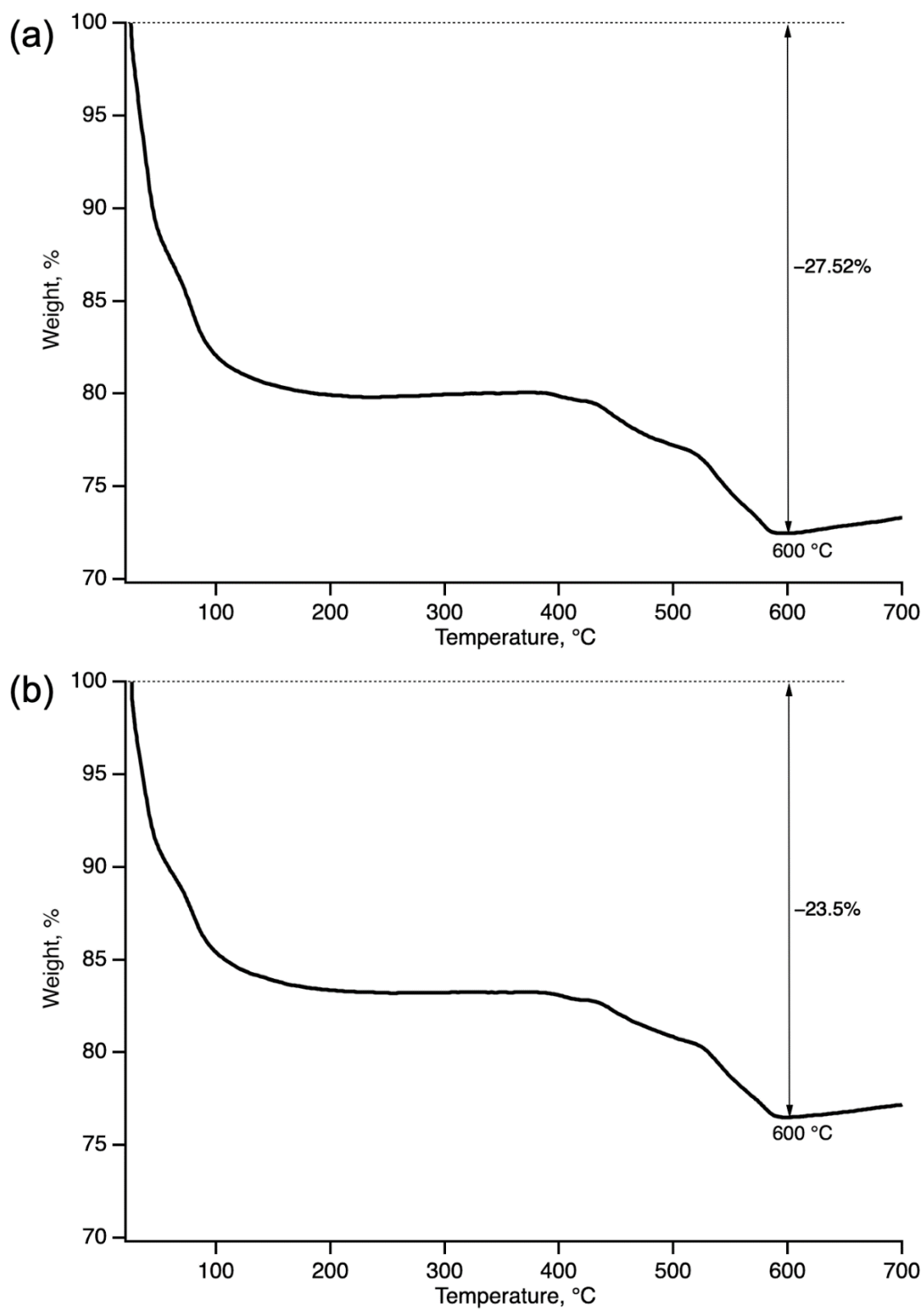


Figure S3. Thermograms of (a) freshly prepared crystals and (b) five-day-aged crystals of 2-Co.

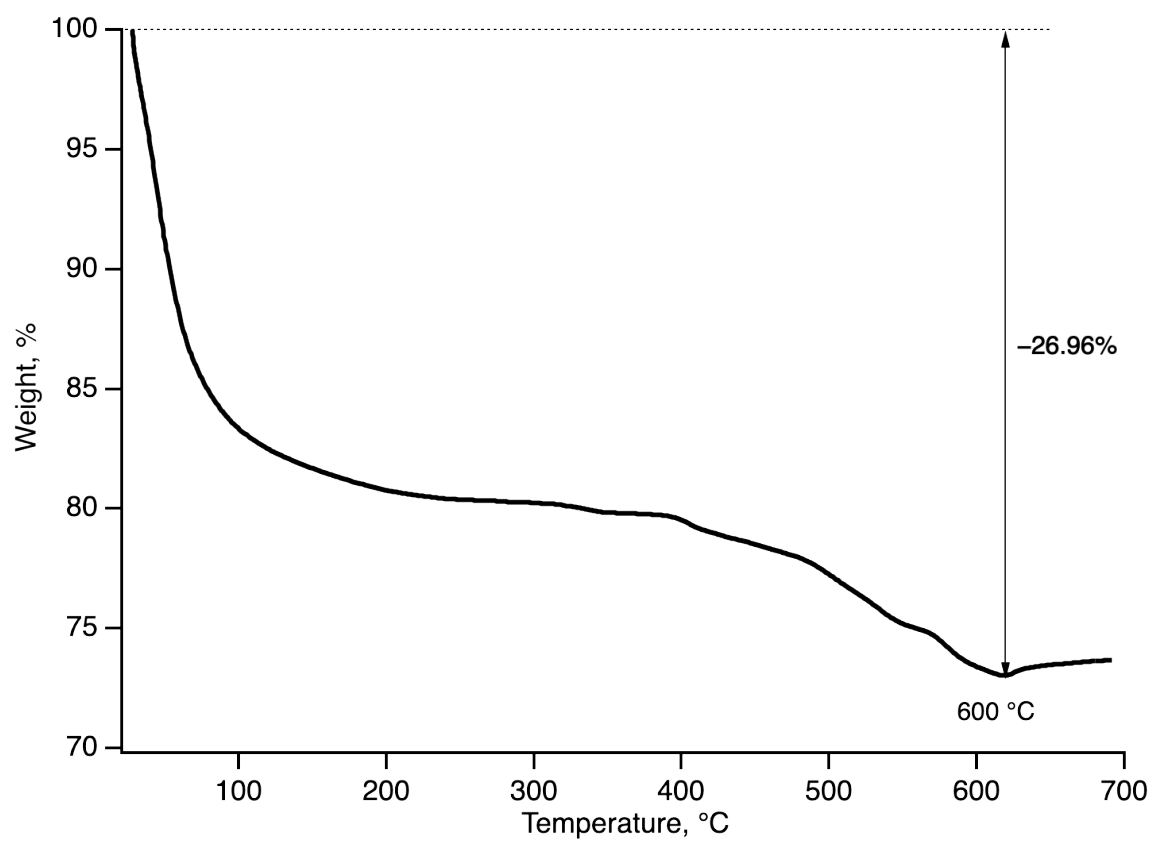


Figure S4. Thermogram of 2-Ni

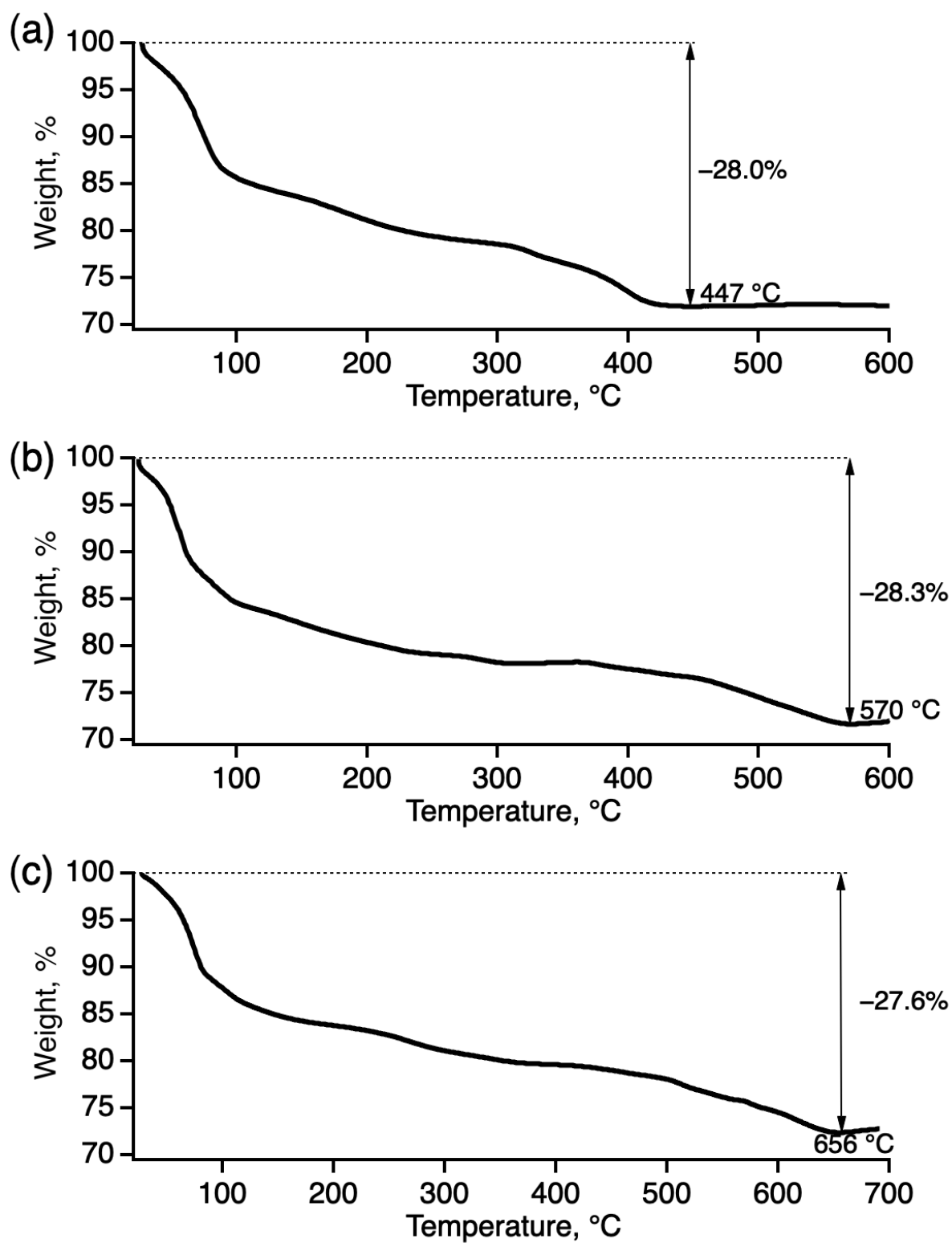


Figure S5. Thermograms of (a) 3-Cr, (b) 3-Fe, and (c) 3-In.

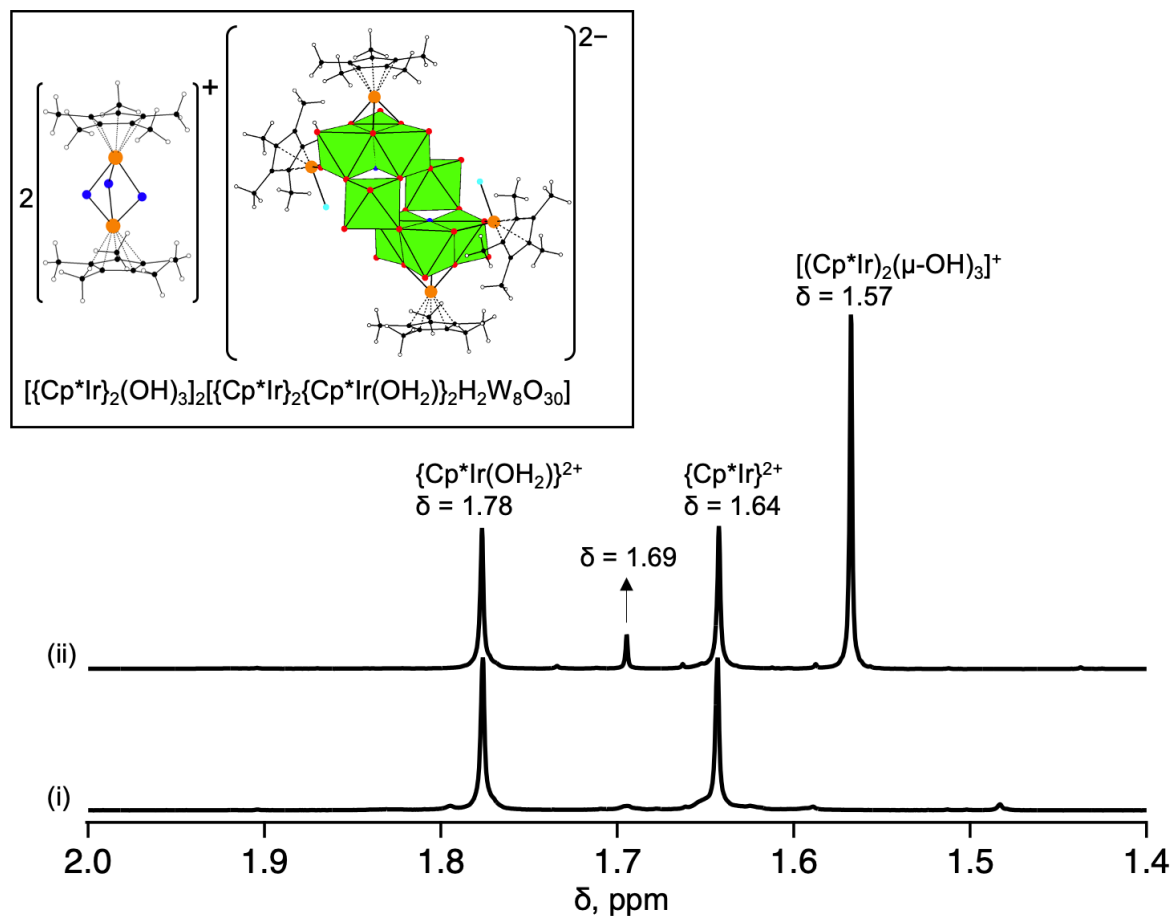


Figure S6. ^1H NMR spectra of **1** (trace i) and (ii) $[(\text{Cp}^*\text{Ir})(\mu\text{-OH})_3]_2[\{\text{Cp}^*\text{Ir}(\text{OH}_2)\}_2(\text{Cp}^*\text{Ir})_2\text{H}_2\text{W}_8\text{O}_{30}]$ (structure shown in the inset) in $(\text{CD}_3)_2\text{SO}$. The signal at 1.69 ppm is most likely due to impurities produced from the reaction of the $[(\text{Cp}^*\text{Ir})(\mu\text{-OH})_3]^+$ cations with dimethyl sulfoxide; the $[(\text{Cp}^*\text{Ir})(\mu\text{-OH})_3]^+$ cations are reactive toward organic compounds. Color scheme: green, W; orange, Ir; red, O; blue, OH groups; cyan, OH_2 ligands; black, C; hollow circles, H.

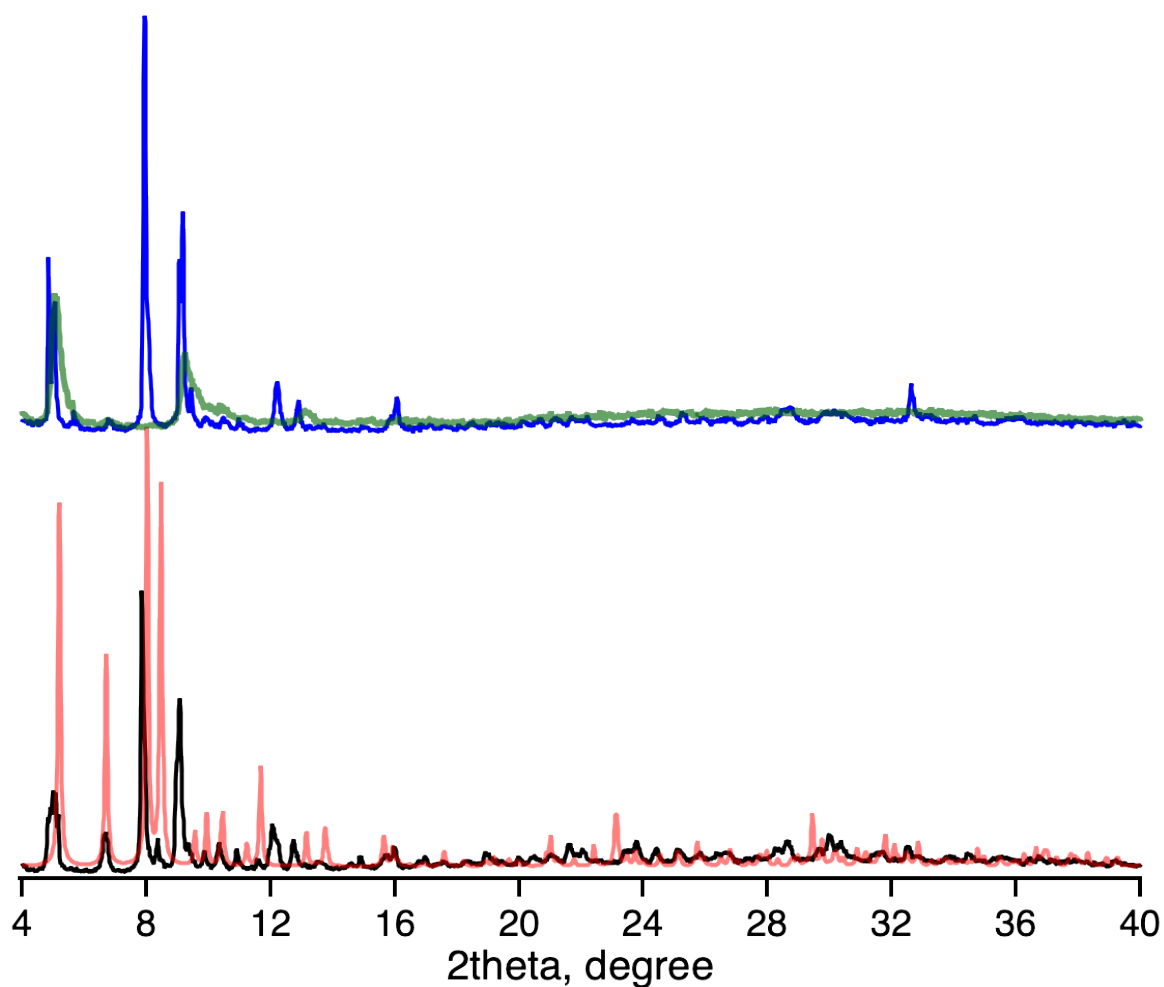


Figure S7. PXRD patterns of **2-Co** synthesized using cobalt(II) sulfate (black trace) and cobalt(II) nitrate (blue trace) in comparison with the simulated pattern using single-crystal data of **2-Co** (transparent red trace). The transparent green trace is a PXRD pattern of the aged powders of **2-Co** synthesized using cobalt(II) nitrate. As such, the discrepancy between the observed and simulated pattern is most likely caused by the evaporation of the crystallization water.

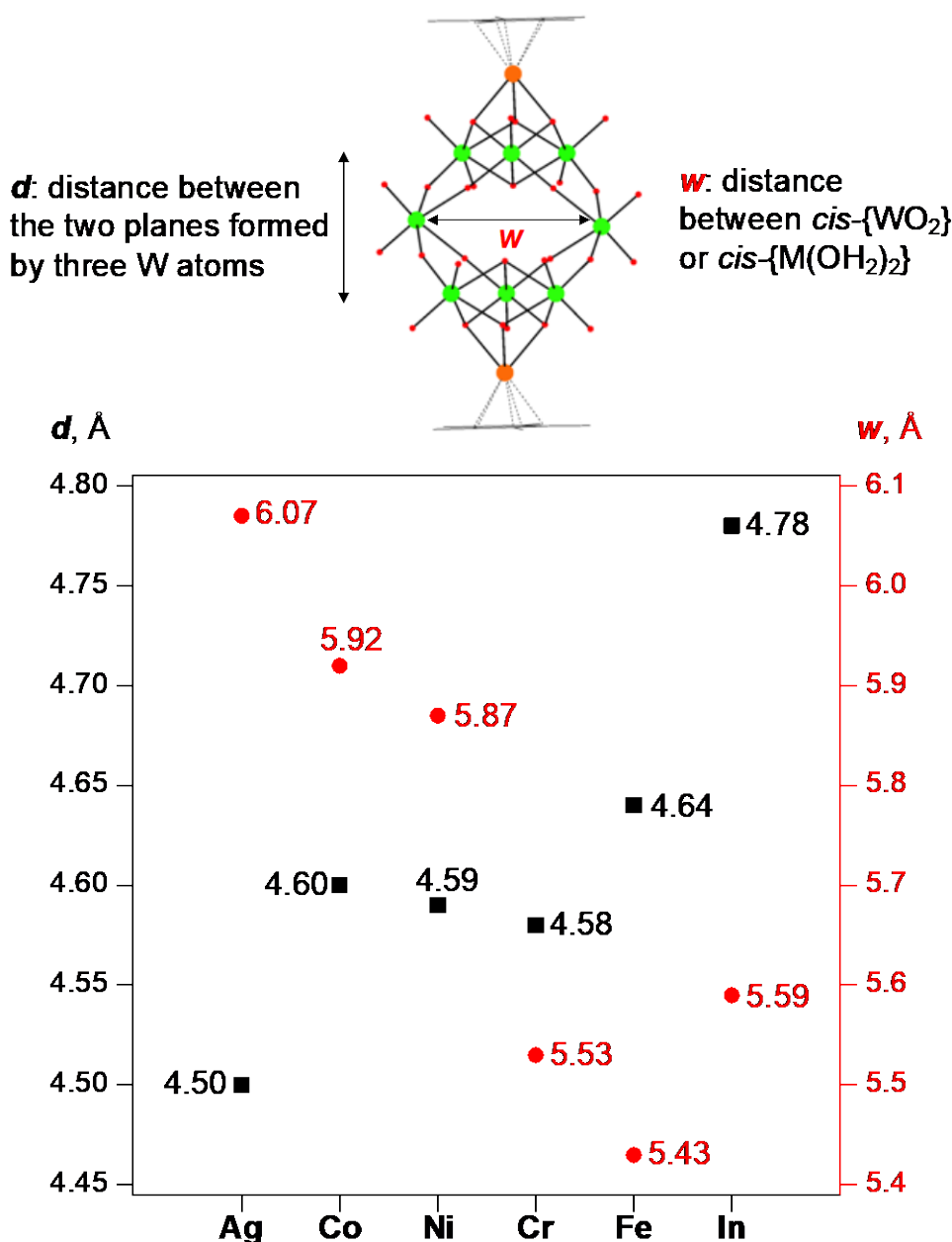


Figure S8. Plot showing the interlayer distance (d , black squares) and the M \cdots M distance between two *cis*-{WO₂} or two *cis*-{M(OH₂)₂} units (w , red dots).

The distance between interlayer W₃ planes (indicated as d) and the distance between the *cis*-{WO₂}/{M(OH₂)₂} units (i.e., the “width” of the molecule, measured as the M \cdots M separation, indicated as w) slightly change depending on the type (particularly the ionic radii) of transition metal cations. For example, the Shannon ionic radii of In³⁺ (0.8 Å), Fe³⁺ (0.645 Å, high-spin), and W⁶⁺ (0.6 Å) can be used to explain the d order of **3-In** > **3-Fe** > **1**. Although our current data is not conclusive in revealing how the M \cdots M distances affect the reactivity, we observed a trend: as the interlayer distance (d) expands, the “width” of the molecule (w) decreases.

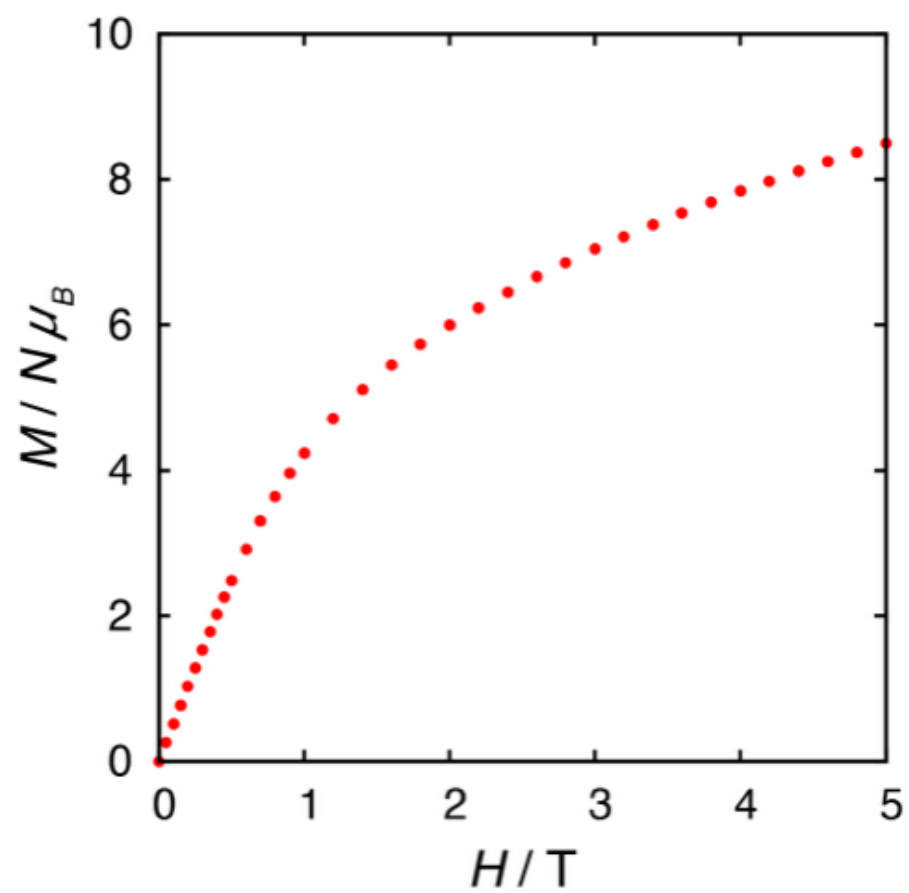


Figure S9. Magnetization curve of **3-Fe**.

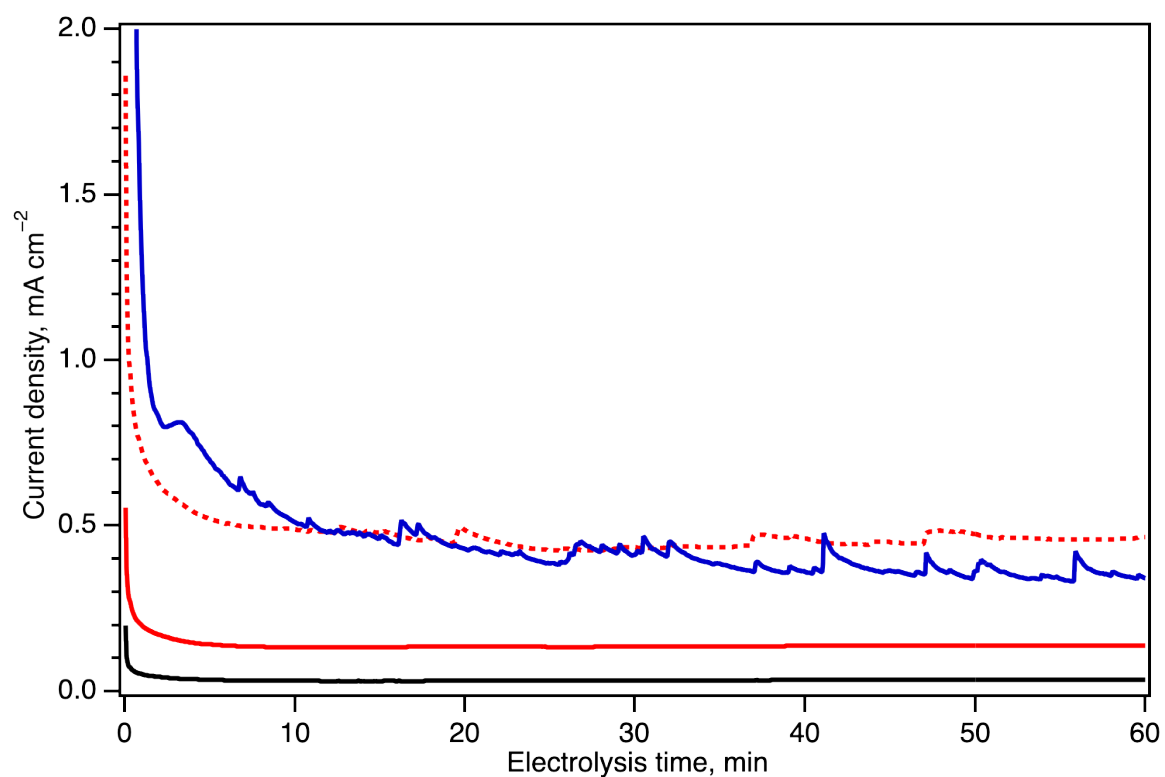


Figure S10. Current–time plot showing current generated over 1 h of controlled-potential electrolysis of 10 wt% **2-Co**/carbon-paste (solid red trace) and 30 wt% **2-Co**/carbon-paste (dotted red trace) in comparison with 10 wt% CoO/carbon-paste (black trace) and 10 wt% Co(OH)₂ (blue trace).

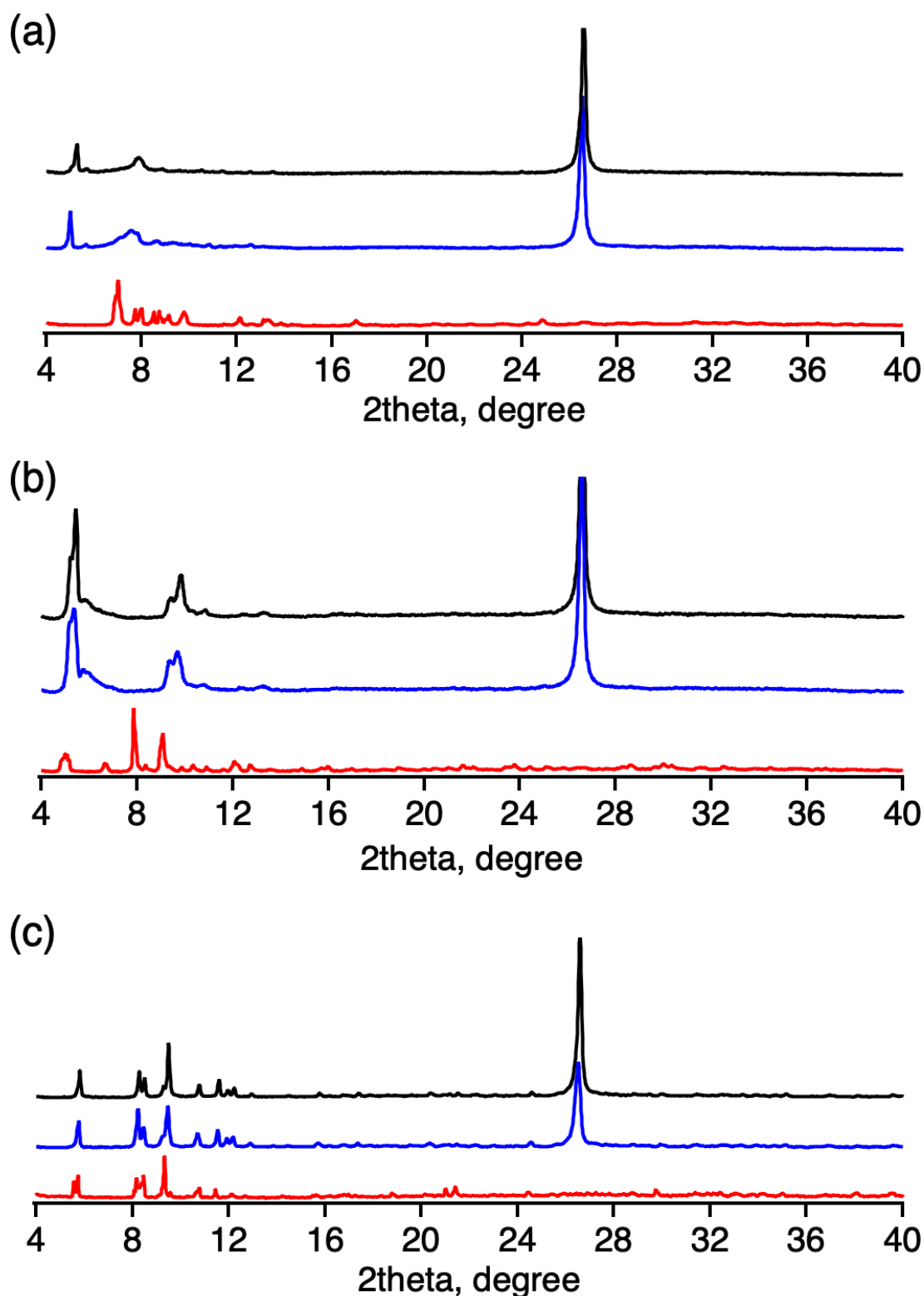


Figure S11. PXRD patterns of the carbon-paste mixtures of (a) **1**, (b) **2-Co**, and (c) **3-Fe** before (blue traces) and after (black traces) controlled-potential electrolysis in comparison with the pattern of their respective pristine solids without carbon paste (red traces). Note that the PXRD pattern of **1** and **2-Co** changes by mixing with carbon paste owing to the loss of lattice water. The intense peak around $2\theta = 26.5^\circ$ arises from the carbon paste. In the PXRD patterns of **1**/carbon-paste before and after electrolysis, peaks below $2\theta = 6^\circ$ were due to impurities; we did not observe similar peaks on other batches of **1**/carbon-paste mixture.

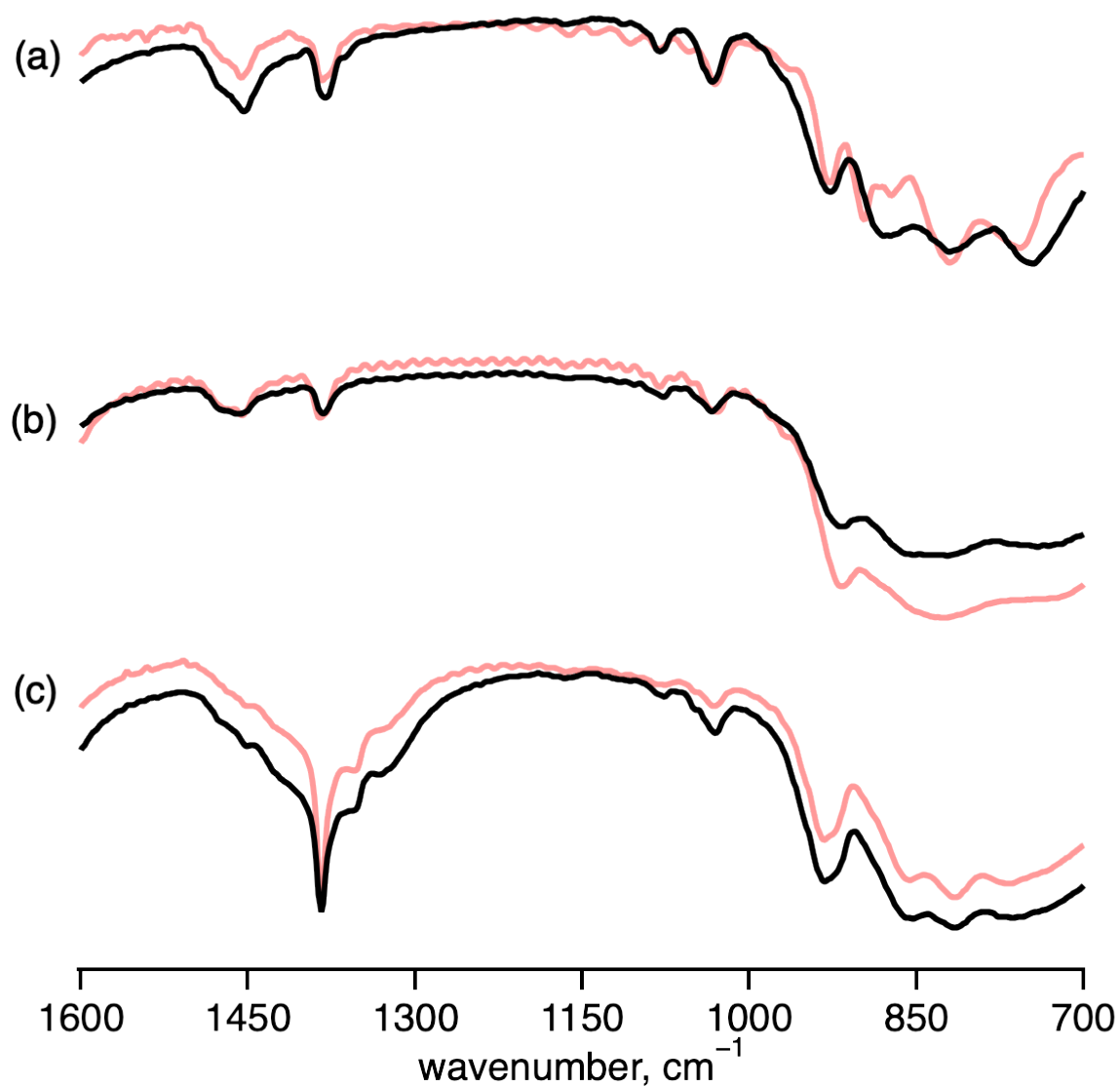


Figure S12. FT-IR spectra of (a) **1**, (b) **2-Co**, and (c) **3-Fe** recovered from the carbon paste mixture after electrolysis (solid black traces) in comparison with the spectra of their respective pristine solids. The compounds were recovered from the carbon paste mixtures by repeatedly sonicating the mixture in acetone.